

# **SAGE III Algorithm Theoretical Basis Document (ATBD) Aerosol Data Products**



**Compiled by the SAGE III ATBD Team**

**LaRC 475-00-105  
Version 1.2  
18 February 2000**

## TABLE OF CONTENTS

<b>1.0 INTRODUCTION.....</b>	<b>1</b>
1.1 PURPOSE.....	1
1.2 SCOPE.....	1
1.3 APPLICABLE DOCUMENTS .....	2
1.3.2 SAGE III ATDB Reference Documents.....	2
1.4 REVISION HISTORY .....	2
1.5 CONTRIBUTING AUTHORS.....	3
1.6 SAGE III STANDARD DATA PRODUCTS.....	4
<b>PRODUCT NAME.....</b>	<b>4</b>
<b>ACCURACY.....</b>	<b>4</b>
<b>2.0 BACKGROUND.....</b>	<b>5</b>
2.1 EXPERIMENTAL OBJECTIVES.....	5
2.2 RELEVANCE OF AEROSOL MEASUREMENTS TO EOS.....	6
2.3 HISTORICAL PERSPECTIVE AND HERITAGE .....	9
2.3.1 Stratospheric Aerosols.....	9
2.3.2 Tropospheric Aerosols.....	12
2.3.3 Upper Tropospheric Clouds.....	14
<b>3.0 ALGORITHM DESCRIPTION.....</b>	<b>20</b>
3.1 INTRODUCTION.....	20
3.1.1 Physical Description.....	20
3.1.2 The Forward Problem.....	23
3.2 RETRIEVAL ALGORITHM DESCRIPTION .....	24
3.2.1 Overview and Assumptions.....	24
3.2.2 Species Separation Algorithm.....	26
3.3 ALGORITHM TESTING REQUIREMENTS .....	33
3.4 VALIDATION PLAN .....	33
3.5 QUALITY CONTROL AND DIAGNOSTICS .....	34
<b>4.0 REFERENCES.....</b>	<b>35</b>
<b>APPENDIX A. SAGE III INSTRUMENT DESCRIPTION.....</b>	<b>44</b>
<b>APPENDIX B. IMPLIMENTATION OF ATMOSPHERIC RETRIEVAL.....</b>	<b>ERROR! BOOKMARK NOT DEFINED.</b>
<b>APPENDIX C. ATMOSPHERIC INHOMOGENEITY.....</b>	<b>52</b>
<b>APPENDIX D. MOLECULAR ABSORPTION CROSS-SECTIONS: SPECTROSCOPIC CONSIDERATIONS FOR SAGE III.....</b>	<b>56</b>
D.1 INTRODUCTION .....	56
D.2 SPECIES SPECIFIC INFORMATION .....	56
D.2.1 Ozone.....	56
D.2.2 Nitrogen Dioxide.....	60
D.2.3 Oxygen.....	63
D.2.4 Water Vapor.....	64
D.2.5 The Nitrate Free Radical NO <sub>3</sub> .....	66
D.2.6 Symmetric Chlorine Dioxide OClO.....	68
<b>APPENDIX E. LUNAR ALTITUDE REGISTRATION.....</b>	<b>70</b>



## **1.0 Introduction**

### **1.0 Introduction**

The Stratospheric Aerosol and Gas Experiment III (SAGE III) is a critical part of the Earth Observing System (EOS). The EOS mission is to develop an understanding of the total Earth system and the effects of natural and human-induced changes on the global environment. SAGE III provides limb occultation measurements with a flexible instrument design that permits on orbit reprogramming and channel selection with up to 800 channels spanning the ultraviolet, visible, and near infrared (280-1040 nm). Solar observations will provide high resolution vertical profiles of multi-wavelength aerosol extinction, the molecular density of ozone, nitrogen dioxide, and water vapor, as well as profiles of temperature, pressure, and cloud presence. In addition, the inclusion of a repositionable solar attenuator will allow lunar occultation observations that will improve the geographic coverage and permit measurements of nitrogen trioxide and chlorine dioxide in addition to ozone, nitrogen dioxide, water vapor, and pressure.

### **1.1 Purpose**

This Algorithm Theoretical Basis Document (ATBD) describes the algorithms used to retrieve the SAGE III aerosol data products. All SAGE III data products will be archived at the NASA Langley Research Center Distributed Active Archive Center (DAAC). The aerosol products consist of aerosol extinction at 9 wavelengths between 385 and 1550 nm, 1020 nm extinction relative to molecular (or Rayleigh) extinction, and stratospheric optical depth at all 9 wavelengths. This document identifies sources of input data which are required for the retrieval; provides the physical theory and mathematical background underlying the use of this information in the retrievals; describes practical considerations affecting algorithm development; and outlines a test and validation approach. However, since the retrieval of each data product depends on the form and quality of the transmission measurements (Level 1B data products) and influences other data retrievals, an overall description of the entire retrieval process is described at a high-level in Chapter 3.

### **1.2 Scope**

An individual document has been developed for each SAGE III standard data product summarized in Table 1.2.1. This document covers the algorithm theoretical basis for the parameters to be included in the SAGE III Data Products at or near launch time. Only parameters that are to be routinely retrieved at the DAAC are discussed. Current development and prototyping efforts may result in modifications to parts of certain algorithms. Only the algorithms which are implemented at the DAAC for routine processing of SAGE III data will be preserved in the a release of this document.

## **1.3 Applicable Documents**

### **1.3.1 Controlling Documents**

Mission to Planet Earth Strategic Enterprise Plan 1996-2002, NASA HQ EOS, May 1996.  
Execution Phase Project Plan for Earth Observing System (EOS), GSFC 170-01-01, Rev. A., May 1995.

### **1.3.2 SAGE III ATDB Reference Documents**

SAGE III Algorithm Theoretical Basis Document: Transmission Data Products, LaRC 475-00-108, February 2000.

SAGE III Algorithm Theoretical Basis Document: Temperature and Pressure Data Products, LaRC 475-00-104, February 2000.

SAGE III Algorithm Theoretical Basis Document: Aerosol Data Products, 475-00-105, February 2000.

SAGE III Algorithm Theoretical Basis Document: Nitrogen Dioxide Data Products, LaRC 475-00-101, February 2000.

SAGE III Algorithm Theoretical Basis Document: Nitrogen Trioxide Data Products, LaRC 475-00-102, February 2000.

SAGE III Algorithm Theoretical Basis Document: Chlorine Dioxide Data Products, LaRC 475-00-103, February 2000.

SAGE III Algorithm Theoretical Basis Document: Water Vapor Data Products, LaRC 475-00-100, February 2000.

SAGE III Algorithm Theoretical Basis Document: Cloud Presence Data Products, LaRC 475-00-106, February 2000.

SAGE III Algorithm Theoretical Basis Document: Ozone Data Products, LaRC 475-00-107, February 2000.

## **1.4 Revision History**

The original version of this document was dated November 15, 1996. Version 1.1 was released on 15 April 1997. This release, version 1.2, is dated 18 February 2000.

## 1.5 Contributing Authors

Each of the SAGE III ATBDs was drafted by a team of SAGE III science team members and SAGE III science cadre, led by one of the science team members. The entire team participated in oral and written revisions of the methodology and documentation as part of the SAGE III science team meetings and research activities.

Contributing Authors	Affiliation
Er-Woon Chiou	SAIC
William P. Chu, Associate PI	NASA Langley Research Center
Albert A. Chernikov	Central Aerological Observatory
Derek M. Cunnold	Georgia Tech
John DeLuise	NOAA
Philip A. Durkee	Naval Postgraduate School
Nikolai F. Elansky	Russian Academy of Science
Benjamin M. Herman	University of Arizona
Peter V. Hobbs	University of Washington
Geoff S. Kent	Science and Technology Corporation
Jacqueline Lenoble	University de Lille, France
M. P. McCormick, Principal Investigator	Hampton University
Alvin J. Miller	NOAA/NCEPS
Volker Mohnen	SUNY at Albany
Randy Moore	SAIC
Michael Pitts	NASA Langley Research Center
Lamont R. Poole	NASA Langley Research Center
Venkatachalam Ramaswamy	Princeton University
David Rind	Goddard Institute for Space Studies
David Risley	SAIC
Michael W. Rowland	SAIC
Philip B. Russell*	NASA Ames Research Center
Vinod K. Saxena	North Carolina State University
Eric P. Shettle	Naval Research Laboratory
Larry W. Thomson*	NASA Langley Research Center
Charles R. Trepte	NASA Langley Research Center
Gabor Vali	University of Wyoming
Lelia B. Vann	NASA Langley Research Center
Pi-Huan Wang	Science and Technology Corporation
Steven C. Wofsy	Harvard University
David C. Woods	NASA Langley Research Center
Joseph M. Zawodny	NASA Langley Research Center

Technical assistance was provided by Susan Walters and Jackie Bumgartner.

\*Lead Authors

## 1.6 SAGE III Standard Data Products

**Table 1.2.1 SAGE III Standard Data Products**

<b>PRODUCT NAME</b>	<b>ACCURACY Absolute :: Relative</b>	<b>TEMPORAL RESOLUTION N</b>	<b>HORIZONTAL Resolution :: Coverage</b>	<b>VERTICAL Resolution :: Coverage</b>
Level 1B Transmission ( $\leq 80$ wavelengths) Solar Events	0.05% :: 0.05%	1/(2 minutes), 30/day	<2 x <1 deg :: Global	0.5 km :: 0-100 km
Aerosol Extinction Strat. Optical Depth (at 9 wavelengths), Aerosol to molecular/extinction ratio at 1020 nm (solar only)	5% :: 5%	1/(2 minutes), 30/day	<2 x <1 deg :: Global	0.5 km :: 0-40 km
H <sub>2</sub> O Concentration (Alt.) Mixing Ratio (Pressure)	10% :: 15%	1/(2 minutes), 30/day	<2 x <1 deg :: Global	0.5 km :: 0-50 km 24 levels/decade :: 1000-0.8 hPa
NO <sub>2</sub> Concentration (Alt.) Mixing Ratio (Pressure) Slant Path Col. Amt. (Alt.)	10% :: 15%	1/(2 minutes), 30/day	<2 x <1 deg :: Global	0.5 km :: 10-50 km 24 levels/decade :: 250-0.8 hPa 0.5 km :: 10-50 km
NO <sub>3</sub> (Lunar Only) Concentration (Alt.) Mixing Ratio (Pressure)	10% :: 10%	1/(2 minutes), $\leq 30$ /day	<2 x <1 deg :: Global	0.5 km :: 20-55 km 24 levels/decade :: 50-0.4 hPa
O <sub>3</sub> Concentration (Alt.) Mixing Ratio (Pressure) Slant Path Col. Amt. (Alt.)	6% :: 5%	1/(2 minutes), 30/day	<2 x <1 deg :: Global	0.5 km :: 6-85 km 24 levels/decade :: 500-0.004 hPa 0.5 km :: 50-85 km
OCIO (Lunar Only) Concentration (Alt.) Mixing Ratio (Pressure)	25% :: 20%	1/(2 minutes), $\leq 30$ /day	<2 x <1 deg :: Global	0.5 km :: 15-25 km 24 levels/decade :: 121-25 hPa
Pressure	2% :: 2%	1/(2 minutes), 30/day	<2 x <1 deg :: Global	0.5 km :: 0-85 km
Temperature Profile	2K :: 2K	1/(2 minutes), 30/day	<2 x <1 deg :: Global	0.5 km :: 0-85 km 24 levels/decade :: 1000-0.004 hPa
Cloud Presence	N/A	1/(2 minutes), 30/day	<2 x <1 deg :: Global	0.5 km :: 6-30 km

## 2.0 Background

SAGE III is the fifth generation of solar occultation instruments designed to measure atmospheric aerosols and gaseous species in the atmosphere. The solar occultation method employs the attenuation of the Sun's rays as observed through the limb of the Earth's atmosphere to determine the vertical distribution of important atmospheric constituents. Measurements are made during each sunrise and sunset (an "event") encountered by the spacecraft (~30/day). This method is well-suited for long-term monitoring of trends and variability in key species such as ozone since the instrument is recalibrated during each event. The instrument concept originated as a hand-held, single wavelength sunphotometer (Stratospheric Aerosol Measurement or SAM) which was flown onboard an Apollo mission in 1975 (Pepin and McCormick, 1976). SAM II was a one wavelength (1000 nm) instrument which operated on Nimbus-7 between 1978 and 1994 (McCormick et al., 1979, 1981). The Stratospheric Aerosol and Gas Experiment (SAGE) operated on the Application Explorer Mission 2 (AEM-2) spacecraft between 1979 and 1981. This instrument made measurements at 4 wavelengths and measured molecular density profiles of O<sub>3</sub> and NO<sub>2</sub> in addition to aerosol extinction at 2 wavelengths (450 and 1000 nm) (McCormick et al., 1979). SAGE II has operated on the Earth Radiation Budget Satellite (ERBS) since 1984 and makes measurements at 7 wavelengths. In addition to the species measured by SAGE, SAGE II measures the molecular density profile of H<sub>2</sub>O and aerosol extinction at 4 wavelengths (385, 453, 525 and 1020 nm) (Mauldin, 1985 McCormick, 1987). In SAGE III, a charged coupled device (CCD) linear array provides spectral coverage from 280 to 1040 nm. In addition, a single photodiode adds aerosol extinction measurements at 1550 nm. (McCormick et al., 1991; Mauldin et al., 1989; McCormick et al., 1993). A repositionable solar attenuator will permit both solar and lunar occultation measurements, increasing the geographical coverage and allowing for the detection of nitrogen trioxide and chlorine dioxide. The incorporation of the CCD array will permit the measurement of gaseous species from multichannel absorption signatures simplifying the retrieval process, and 16-bit digitization will improve the precision and altitude range of the measurements.

### 2.1 Experimental Objectives

The science objectives to be accomplished by SAGE III are:

- Retrieve global profiles of atmospheric aerosol extinction, temperature, and pressure and molecular density profiles of ozone, water vapor, nitrogen dioxide, nitrogen trioxide, and chlorine dioxide with 0.5 km vertical resolution;
- Characterize tropospheric as well as stratospheric clouds and investigate their effects on the Earth's environment, including radiative, microphysical, and chemical interactions;



- Determine long-term trends in gaseous species and temperature;
- Provide atmospheric data essential for the interpretation and calibration of other satellite sensors, including EOS instruments.
- Investigate the spatial and temporal variability of these species in order to determine their role in climate processes, biogeochemical cycles, and the hydrological cycle.

## **2.2 Relevance of Aerosol Measurements to EOS**

Aerosol play a significant role in the radiative and chemical processes governing the Earth's climate. These effects are illustrated in Figure 2.2.1. In addition, aerosols may also influence measurements of other atmospheric, oceanic, and solid Earth parameters (e.g., Bandeen and Fraser, 1982). National and international bodies (e.g., Hobbs, 1994; Bates and Gras, 1994; Charlson and Heintzberg, 1995; IPCC, 1995; NRC, 1994, 1996) have called for increased efforts to measure aerosol properties and effects, as a means of improving predictions of future climate (including greenhouse warming, ozone depletion, cloudiness, and radiation exposure of living organisms) and enhancing the information retrieved from a wide variety of remote measurements. SAGE III will make the high-quality aerosol measurements which are crucial to adequately address these issues. SAGE III's contribution to EOS is enhanced by continuing the aerosol measurements provided by SAM II, SAGE, and SAGE II.

Examples of science issues which require high quality, global aerosol measurements include:

### **Aerosol variability and Ozone Trends**

Recent work by Solomon et al. [1996] demonstrates that the variability of aerosol loading over the past 20 years has played a significant role in the destruction of ozone in the lower stratosphere. In fact, the influence of the variations in aerosol loading is sufficiently large that proper interpretation of the observed trend in total ozone must take into account concurrent aerosol variations. In addition, the impact of aircraft exhaust on ozone is strongly dependent on the abundance and properties of the ambient aerosol. Specifically, while current predictions of the aerosol-enabled ozone depletion resulting from a fleet of High Speed Civil Transport (HSCT) aircraft are made smaller than those a few years ago, significant uncertainties remain, and there is a need for improved understanding of stratospheric and upper tropospheric aerosol abundance, composition, and physical state [Stolarski and Wesoky, 1993; NRC, 1994].

### **Climate Forcing by Aerosols**

Estimates of the climate impact of the aerosol associated with the June 1991 Pinatubo eruption which resided primarily in the stratosphere, and tropospheric aerosols have combined to highlight the need for improved understanding of tropospheric and stratospheric aerosol effects on climate. Aerosol radiative forcing is one of the largest sources of uncertainty in validating current climate models and predicting future climate

[IPCC, 1995, 1996]. A newly-proposed multiagency program designed to improve climate predictions specifically calls for improved satellite measurements to provide a geographically and vertically resolved climatology of aerosol extinction throughout the troposphere and stratosphere [NRC, 1996].

### **Remote Measurement Science**

Remote measurements of such diverse properties as sea surface temperature, vegetation type and condition, and atmospheric trace gases have all been adversely affected by the presence of aerosols during various tropospheric and stratospheric aerosol conditions in the past. Independent measurements of aerosols, such as provided by the SAM/SAGE series, have been used to improve retrievals of diverse properties from other sensors, and this will continue in the future. Even future EOS sensors designed to retrieve tropospheric aerosol properties, such as MISR and MODIS, have cited the need for SAGE III measurements of stratospheric aerosols as a means of improving the accuracy of their retrievals [e.g. MISR, 1995; Diner *et al.*, 1989; Martonchik and Diner, 1992; Wang and Gordon, 1994; King *et al.*, 1992].

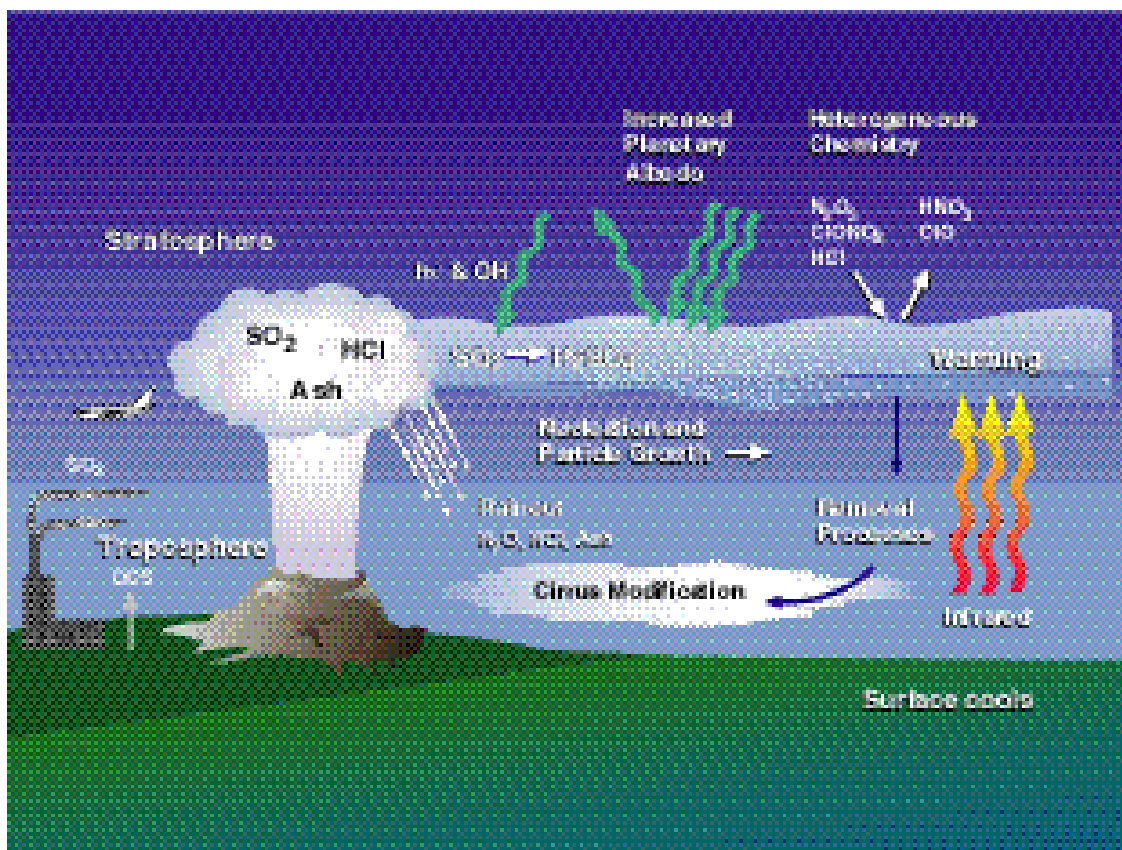


**Figure 2.2.1** As shown in the above schematic, a volcanic eruption can produce a significant perturbation to the Earth-Atmosphere system by injecting material into the stratosphere where, depending on the magnitude and altitude of the injection, it may persist for several years. The material injected into the stratosphere may include ash, which typically does not remain for more than a few months, and gaseous components including water vapor, sulfur dioxide, and hydrochloric acid. Hydrochloric acid is mostly dissolved into condensing water vapor and rains out of the original cloud. Aerosols are produced when the sulfur dioxide ( $\text{SO}_2$ ) is chemically transformed into sulfuric acid ( $\text{H}_2\text{SO}_4$ ) which rapidly condenses into aerosols since it has a very low saturation vapor pressure. The new aerosol increases the Earth's albedo by reflecting solar radiation back into space and can warm the stratosphere by absorbing upwelling infrared radiation. Sedimentation and atmospheric circulation eventually transport the aerosol into the troposphere where they may modify cloud optical properties (particularly cirrus) and further modify the Earth's radiative processes. An additional impact of an eruption is the increased efficiency of heterogeneous chemical processes (i.e., ones that take place on the surface of aerosols). This is coupled with the human-modification of increasing stratospheric chlorine which lead to ozone destruction is produced by modifying reactive chlorine and nitrogen chemistry. This process is similar to that produces the Antarctic ozonehole except the surface is provided by polar stratospheric clouds. Increased stratospheric chlorine levels have been linked to industrially-produced chlorofluorocarbons (CFCs).

## 2.3 Historical Perspective And Heritage

### 2.3.1 Stratospheric Aerosols

Since 1978, monitoring of the spatial distribution and variability of stratospheric aerosol has been carried out by the SAM/SAGE family of spaceborne instruments as well as various other remote and in situ measuring systems [e.g. Osborn *et al.*, 1995; Grainger *et al.*, 1993; Hervig *et al.*, 1993; Wilson *et al.*, 1993; Pueschel *et al.*, 1989, 1992, 1994; Deshler *et al.*, 1992; 1993]. Over this period, the primary source of stratospheric aerosol variability has been periodic injections of aerosol or gaseous aerosol precursors such  $\text{SO}_2$  due to volcanic eruptions. In general, stratospheric aerosols are produced in situ by processes that include the photochemical oxidation of gaseous  $\text{SO}_2$  into  $\text{H}_2\text{SO}_4$  vapor, followed by condensation and microphysical processes (e.g. coagulation and sedimentation) that yield the observed aerosol. The composite SAM II/SAGE/SAGE II record of stratospheric aerosol 1- $\mu\text{m}$  optical depth (Figure 2.3.1.1) shows the large effects of the eruptions of El Chichon in 1982 and Mount Pinatubo in 1991, as well as those of smaller eruptions such as Mount St. Helens in 1980, Nevada del Ruiz in 1985, and Kelut in 1990 [McCormick *et al.*, 1993].

The majority of ambient stratospheric aerosols can be represented reasonably well as spherical liquid droplets whose composition by weight at normal stratospheric temperatures is between 50 and 90%  $\text{H}_2\text{SO}_4$  with the remainder consisting of primarily  $\text{H}_2\text{O}$ . While the most significant source of stratospheric aerosols is explosive volcanic activity, a non-volcanic background level of stratospheric aerosols may result from the diffusion into the stratosphere of carbonyl sulfide (OCS) originating in the troposphere [Crutzen, 1976]. However, recent research [Chin and Davis, 1995] suggests that OCS is unlikely to have produced even the lowest levels of stratospheric aerosols (1979) observed since 1978. It has also been suggested that a 5% annual increase in the non-volcanic background stratospheric aerosol mass occurred over the period from 1978 to 1989 [Hofmann, 1990]. It has been speculated that the increase could be related to the increase in sulfur emissions from commercial aircraft or other anthropogenic sources [Hofmann, 1991]. Although more recent evaluations tend to argue against this increase [Thomason *et al.*, 1996], it is nonetheless clear that the viability of current national technological policy, including the proposed stratospheric aircraft fleet, is dependent on quantifying long-term trends in the background aerosol loading.

Aspects of the morphology of stratospheric aerosols, including their sources, sinks, and distribution, have been described by several researchers [e.g., Turco *et al.*, 1982; Mohnen *et al.*, 1990; Trepte *et al.*, 1993; Kent *et al.*, 1995]. As a result of recent low-latitude, high-altitude injections of aerosol, the aerosol distribution since 1978 has had shows a maximum in the tropics centered at an altitude between 20 and 27 km. Since there is an impedance to meridional transport due to the strong horizontal wind shear in the subtropics, the tropical maximum is long-lived and acts as an effectively permanent (albeit decreasing) source of aerosol to mid and high latitudes [Trepte and Hitchman, 1992; Thomason *et al.*, 1996]. Non-volcanic sources of stratospheric aerosol such as natural OCS and industrially-derived

SO<sub>2</sub> also act to support the presence of a tropical aerosol reservoir. Within the tropical maximum, the largest stratospheric aerosol particle sizes are generally observed, probably as a result of their long residence time in this region. Outside the tropics, aerosol loading is relatively constant on isentropic surfaces [Trepte *et al.*, 1995]. Smaller particles are generally found in the mid-latitudes, whereas larger particles are found at higher latitudes [Yue and Deepak, 1984]. The occurrence of larger particles near the poles suggests growth through microphysical processes as particles are transported to regions with colder temperatures. In general, the aerosol size distribution can be approximated as a single or multi-modal log-normal [Pinnick *et al.*, 1976; Russell *et al.*, 1981 ; Oberbeck *et al.*, 1989; Russell *et al.*, 1996]. The effective radius of the aerosol size distribution is about 0.1-0.2  $\mu\text{m}$  in background conditions, but can be substantially larger following a volcanic injection of aerosol.

There is a noticeable difference in aerosol distribution between the northern and southern hemispheres, a feature which may be a consequence of hemispheric differences in planetary wave activity and the phasing of periodic transport phenomena associated with the tropical reservoir such as the annual cycle and the Quasi-Biennial Oscillation (QBO). SAGE and SAGE II data show evidence of the extension of stratospheric aerosols into the upper troposphere at mid and high latitudes [Kent *et al.*, 1995]. SAM II, SAGE, and SAGE II have observed a post-winter optical depth minimum in both polar regions that results from both the sedimentation of large polar stratospheric cloud (PSC) particles and large-scale subsidence within the polar vortices into the lower stratosphere and upper troposphere [Thomason and Poole, 1993]. Aerosol observations can also be used to study dynamical processes at high latitudes [e.g., Kent *et al.*, 1985].

Also evident in Figure 2.3.1.1 are seasonal enhancements, especially those in the Antarctic winters. These large increases in stratospheric optical depth are due to PSCs [McCormick *et al.*, 1982]. Although the composition of these clouds is debated, they are probably composed of ice clouds (at the coldest temperatures) and a hydrate of HNO<sub>3</sub> or a ternary solution of HNO<sub>3</sub>, H<sub>2</sub>SO<sub>4</sub>, and H<sub>2</sub>O [Toon *et al.*, 1986; McElroy *et al.*, 1986; Poole and McCormick, 1988]. The cloud particle surfaces provide sites for heterogeneous chemical reactions that transform relatively inert forms of chlorine such as HCl and ClONO<sub>2</sub> into more reactive forms such as Cl<sub>2</sub>. Ultimately, Cl<sub>2</sub> disassociates into Cl\* which in turn is responsible for ozone destruction and the formation of the austral spring ozone hole. A climatology of the occurrence of PSCs in the southern hemisphere derived from 10 years of SAM II observations is shown in Figure 2.3.1.2 [Poole and Pitts, 1994]. The role of PSCs in climate and the observations of PSCs by SAM/SAGE are discussed in greater detail in the SAGE III Cloud Presence ATBD.

Labitzke *et al.* [1983] showed that the El Chichon aerosol, with a peak concentration at 24 km and banded zonally between about 10° S and 30° N (during the first 6 months) warmed this altitude region by a few degrees. This warming was predicted by various models [Hansen *et al.*, 1981; Pollack and Ackerman, 1983; and Robock 1984]. Following the eruption of Mt. Pinatubo, substantial changes in the planetary albedo and surface radiation were observed [Minnis *et al.*, 1991]. In addition, substantial heating in the tropical stratosphere was observed immediately after the eruption. This heating was sufficient to

cause tropical stratospheric temperatures at 30 hPa to increase as much as three standard deviations above the 26-year mean [Labitzke *et al.*, 1992]. Global planetary temperature was observed to decrease in the months following the Pinatubo eruption [Dutton and Christy, 1992; Hansen *et al.*, 1993, 1995; Fiocco *et al.*, 1995].

Probably the most striking SAGE II observations have been those of the spread and evolution of the aerosol cloud from the Mount Pinatubo eruption. As shown in Figure 2.3.1.3, about one month following the eruption, the satellite data showed that aerosols from Pinatubo had spread in a band about the equator and that mid-latitude anticyclones had transported material to high latitudes in both hemispheres. In the Northern Hemisphere, early transport of aerosol out of the tropics occurred preferentially in the upper troposphere and lower stratosphere and was associated with the summer Asian monsoon. In the Southern Hemisphere, early transport occurred primarily between 18 and 24 km and was caused by a large stratospheric anticyclone. SAGE II data show that by 7 months after the eruption, a dense aerosol layer had covered most of the Northern Hemisphere and had reached high southern latitudes as well. The Pinatubo eruption resulted in about 30 Tg of stratospheric aerosol material globally, more than twice that of the El Chichon eruption.

The eruption of Pinatubo provided a nearly 100-fold increase in the surface area available for heterogeneous chemical processing throughout the stratosphere. Significant reductions in NO<sub>2</sub> [Johnston *et al.*, 1992; Koike *et al.*, 1994] along with observations of enhanced HNO<sub>3</sub> [Rinsland *et al.*, 1994] suggested a repartitioning of reactive nitrogen species (e.g., NO<sub>2</sub>) into less reactive forms. More notably, there were many reports of record low ozone levels from the Antarctic [Hofmann *et al.*, 1994] and northern mid-latitudes [Komhyr *et al.*, 1994; Hofmann *et al.*, 1994] which were likely the result of heterogeneous processes. On the other hand, a 6-8% loss of ozone in the tropics immediately after the eruption is more likely the result of lofting associated with the strong stratospheric heating previously discussed [Kinne *et al.*, 1992]. In fact, observations by the Total Ozone Mapping Spectrometer (TOMS) showed a global ozone deficit of nearly 6% by mid-1992 and only a slow recovery after that time [Gleason *et al.*, 1993]. More complete descriptions of the radiative and chemical impacts of the Pinatubo eruption are given by McCormick *et al.* [1995], Kinnison *et al.* [1994], Fiocco *et al.* [1995], and Russell *et al.* [1996]. The poleward transport of the Pinatubo aerosol has been discussed by Trepte *et al.* (1993).

Recent work by Solomon *et al.* [1996] demonstrates that stratospheric aerosol variability strongly influences observed ozone trends during even nominally background aerosol loading periods (Figure 2.3.1.4; Solomon *et al.*, 1996). These results show that it is virtually impossible to correctly interpret long term ozone trends without accounting for stratospheric aerosol variability. These and related results showing the crucial role that stratospheric aerosols play in determining the impact of aircraft exhaust on ozone [Stolarski and Wesoky, 1993; NRC, 1994] provide very strong justification for continued global observations of stratospheric aerosols.

### 2.3.2 Tropospheric Aerosols

Tropospheric aerosols form a much more complex system than those in the stratosphere. The aerosols may be surface derived from both land and ocean or formed in the atmosphere as a result of gas-to-particle conversion or cloud cycling. Once in the atmosphere and they are subject to transport away from their origin, sometimes over very large distances, and they may be removed from the atmosphere by both dry (sedimentation) and wet processes (rainout). In general the aerosol mass concentration decreases with altitude, reaching its lowest values in the upper troposphere. The composition of tropospheric aerosols is quite variable and both internal (within a single particle) and external (between particles) mixtures are formed. In the upper troposphere the composition is generally simpler than in the lower troposphere, sulfur in the form of sulfuric acid or ammonium sulfates becoming increasingly dominant at higher altitudes. For the purpose of behavioral description and modeling, tropospheric aerosols are commonly classified according to composition and source. Aerosol categories include maritime, desert dust, urban, biogenic, etc. Within each category it is possible to assign a typical particle size distribution, composition and refractive index. Several publications describe the climatology of tropospheric aerosols, their classification and their optical and physical properties [WMO, 1983, d'Almeida *et al.*, 1991, Jaenicke, 1993].

Observation of tropospheric aerosols from space may be made by measuring solar radiation scattered back from the atmosphere [e.g., Kaufman, 1995]. Such measurements reveal most clearly the larger and lower-altitude aerosol concentrations such as desert dust clouds and pollution episodes. Converting these measurements to quantitative estimates of aerosol concentration is difficult because of the problem of separating the aerosol signature from that of the background and the presence of multiple scattering. These factors have caused such studies from space of tropospheric aerosols to be largely confined to those over the oceans [Griggs, 1975; Rao *et al.*, 1989; Durkee *et al.*, 1991], although several techniques have been used to retrieve aerosol properties over land [e.g., Kaufman, 1995; Holben *et al.*, 1992]. The SAM/SAGE series of solar occultation satellites, with their limb viewing geometry, have a much greater sensitivity to the presence of aerosols and provide data that is in many ways complimentary to that obtained from nadir viewing instruments. Whereas data from nadir viewing instruments lacks vertical resolution but has good horizontal resolution, that from SAM/SAGE has a good vertical resolution (~ 1 km) and a horizontal resolution of about 200 km. The much greater sensitivity of the SAM/SAGE Instruments combined with the increasing presence of cloud at lower altitudes also means that the best tropospheric data is obtained from these satellite instruments in the upper rather than the lower troposphere.

Despite the presence of optically thick clouds, solar occultation data within the troposphere often extend to within a few kilometers of the Earth's surface. Approximately 50% of SAGE II 1020 nm extinction profiles extend to 5km or below (Figure 2.3.1.5; Wang, 1994). Upper tropospheric data from SAGE, SAGE II, and SAM II have been used to develop a global aerosol climatology for this region (Kent *et al.*, 1988, 1991, 1995). These data show that the two main influences on the upper tropospheric aerosol are

seasonal lofting of material from below, and downward transfer of volcanic aerosol from the stratosphere. Maximum lifting of surface material occurs in local spring in both hemispheres and is observed at all latitudes between 20°N and 80°N, and 20°S and 60°S; the data also shows a significant hemispheric asymmetry with more aerosol in the northern hemisphere. Downward transfer of volcanic aerosol is particularly observed polewards of 40° latitude, where a substantial enhancement of material occurs down to altitudes 2-3 km below the tropopause. This is illustrated in Fig. 2.3.1.6 (Kent, 1996), which contains six panels covering the latitude range from 60°S to 60°N. Each panel shows the variation in SAGE II zonally averaged 1020 nm extinction from 6.5 km to 24.5 km altitude. We can see the penetration of stratospheric volcanic material into the upper troposphere between 1984 and 1988, particularly at high latitudes. Upward extending tongues of extinction, occurring in the spring of each year and more pronounced in the northern hemisphere, are related to the springtime surface derived aerosol enhancements. The asymmetry between hemispheres is also shown in the analysis of April 1983 aerosol optical depth data from AVHRR [Fig. 2.3.1.7, Durkee, 1991]. Although this figure shows the total atmospheric optical depth, including the boundary layer, it strongly resembles the latitudinal behaviors of the upper tropospheric aerosol as determined by SAGE II. The latitudinal variation of the downward transfer of volcanic material as seen in Fig. 2.3.1.6 is consistent with planetary circulation models in which there is uplift at low latitudes and downward transport at high latitudes (WMO, 1985).

Aerosols transported into the middle or high troposphere from either the planetary boundary layer (PBL) or the stratosphere will be readily observable by SAGE III during cloud-free conditions. In combination with water vapor and ozone profiles, these tropospheric aerosol profiles and associated size distributions can be used for the identification of air masses, and to provide information on the exchange of matter between the troposphere and stratosphere. Presently, the observation of middle and high tropospheric aerosols is obtained mainly by a few in situ measurements. Being optically thin, they are not easily monitored by nadir-looking spaceborne instruments. SAGE II can measure aerosols down to the Earth's surface in only the 1020 nm channel which precludes size distribution determinations. SAGE III will provide extinction measurements for at least two wavelengths (1020 and 1550 nm) down to near the Earth's surface, allowing the retrieval of some size distribution information. The middle troposphere will be probed by all wavelengths greater than about 500 nm, however, thereby providing exceptional information on aerosol and cloud characteristics, and their separation.

SAGE III observations offer additional and unique opportunities to attack important scientific problems relating to tropospheric aerosols above the PBL. These include the role of tropospheric aerosols in the Earth's radiation budget, the transport of aerosols into the free troposphere from the industrialized regions of continents and from regions with large-scale biomass burning, and the role of aerosols of stratospheric or boundary layer origin in cloud formation. The radiative properties of aerosols change significantly as the ambient relative humidity changes. Stratospheric aerosols transported and distributed into the upper-troposphere experience such changes in moisture and will grow larger in response to the relative humidity environment that frequently exceeds 60%. Hence, their extinction characteristics change considerably for those particles of stratospheric origin, consisting



mainly of sulfuric acid, that reside in the troposphere. These optical changes can be documented and incorporated into climate models.

SAGE III observations down to the PBL are highly probable, especially in areas of large-scale subsidence. Such observations allow the documentation of photochemically produced haze from precursor gases such as sulfur dioxide, oxides of nitrogen and volatile organic compounds emitted into the atmosphere as by-products of fossil fuel combustion. Typically, these aerosol episodes extend over hundreds of kilometers and occur several times a year over most industrial regions of the globe. A significant fraction of these "urban based" particles are advected into the free troposphere and transported over large distances. Given a suitable sampling opportunity, SAGE III will be able to observe these long-range transport phenomena.

It is anticipated that EOS instruments such as MODIS and HIRIS will provide complementary observations to further strengthen the assessment and conclusions from the SAGE III data sets. Similarly, SAGE III will provide data needed for the more accurate determination of the effects of aerosols on other satellite-borne sensors. For example, stratospheric aerosol enhancements modify measurements of the Earth radiation budget from satellites (e.g., ERBE) and perturb the satellite measurement of sea surface temperatures [Strong, 1984]. One of the experimental products of the AVHRR satellite measurements is optical depth of aerosols over oceans as shown (zonally averaged) in Figure 2.3.1.7. The SAGE III data will be useful for separating the stratospheric aerosol component of the AVHRR optical depth from the total, especially important during conditions of volcanic aerosol enhancements which can be equal to or larger than the tropospheric aerosol component. Another example is the ground-based Umkehr observations of ozone profile that were started in 1958. Stratospheric aerosols affect these measurements and similar ground-based zenith-sky measurements of other gases. However, corrections can be made if aerosol profiles are known. To date, the SAGE data have been the best source of stratospheric aerosol information for these corrections, which are now being routinely done for all Umkehr stations. Umkehr ozone profiles are being used to validate SBUV ozone profile observations and for determining trends between 25 and 45 km. The SAGE II data, for example, are routinely archived at the World Ozone Data Center in Canada for purposes of correcting these data.

### **2.3.3 Upper Tropospheric Clouds**

A major problem in the interpretation of solar occultation data in the troposphere has been the likely presence of cloud along the horizontal path from the Sun to the satellite instrument. This may cause the apparent aerosol extinction to rise by a large factor above that due to the aerosol alone. Separation of the extinction due to cloud from that due to the aerosol along the optical path has been carried out using the differential wavelength characteristics of the extinction due to aerosol and cloud [Kent and McCormick, 1991, Kent *et al.*, 1993]. Cloud, consisting of particles that are large compared to the SAGE II wavelengths shows little or no variation of extinction with wavelength. Aerosols, in particular those forming the tropospheric background, have sizes that are smaller than the

wavelengths used and have an extinction that is wavelength dependent. SAGE II makes measurements at two wavelengths (525 and 10200 nm) from an altitude of 6 km upwards. By comparing the extinction measured at these two wavelengths, it has been possible to separate that due to the aerosol alone from that due to cloud. This technique has been used to create maps of cloud occurrence presently available on the Langley-DAAC. It has also been used to study the seasonal and long-term behavior of upper tropospheric aerosol and to derive estimates for the mass loading and particle size [Kent *et al.*, 1995]. These studies have, for the first time, provided a global look at upper tropospheric aerosol characteristics. In particular, the penetration of volcanic aerosol from the stratosphere into the upper troposphere in middle and high latitudes has been quantified, and regular seasonal springtime enhancements of the upper tropospheric aerosol in both hemispheres have been observed.

The method just described could not be applied to data from SAM II or SAGE, neither of which provided aerosol extinction data at more than one wavelength in the troposphere. It has considerable potential for development and application to data from SAGE III where aerosol measurement will be made at several wavelengths in the upper troposphere and at two wavelengths down to the Earth's surface. Problems have occurred when applying the method to SAGE II data for the upper troposphere following major volcanic eruptions. These have been due to the large size of the aerosol particles then present which show little variation of extinction with wavelength. SAGE III with its extra wavelength 1540 nm will provide extra discrimination against such aerosol. It may also be useful in separating cloud from aerosol in the lower troposphere where larger aerosols also occur.

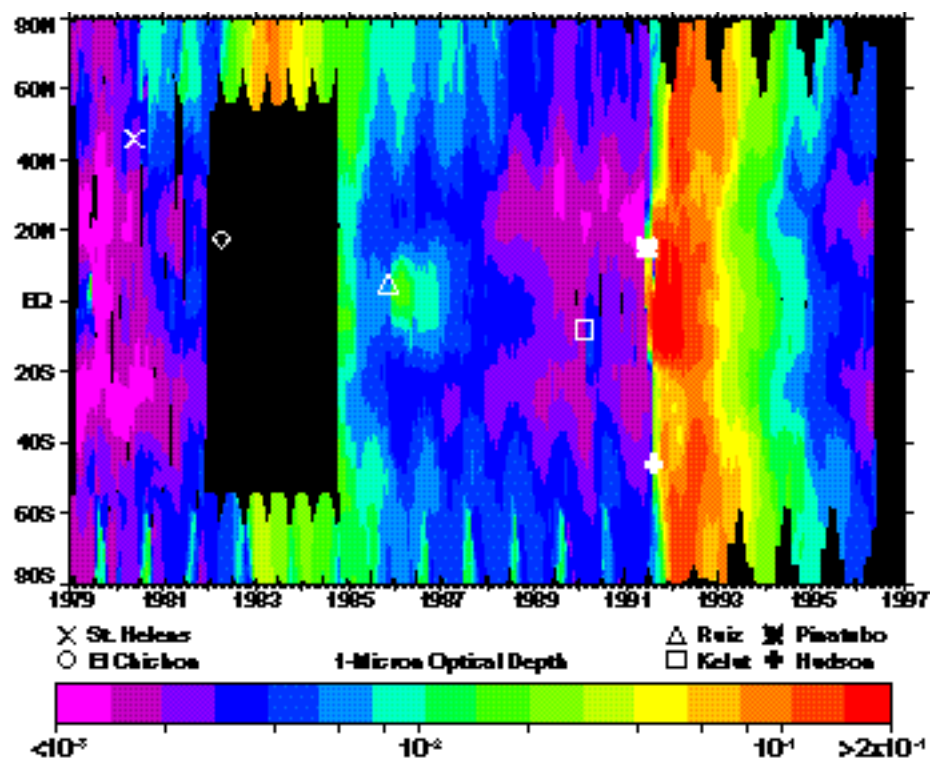


*Figure 2.3.1.1 Time series of SAM II and SAGE I/II stratospheric optical depths (1 micron).*

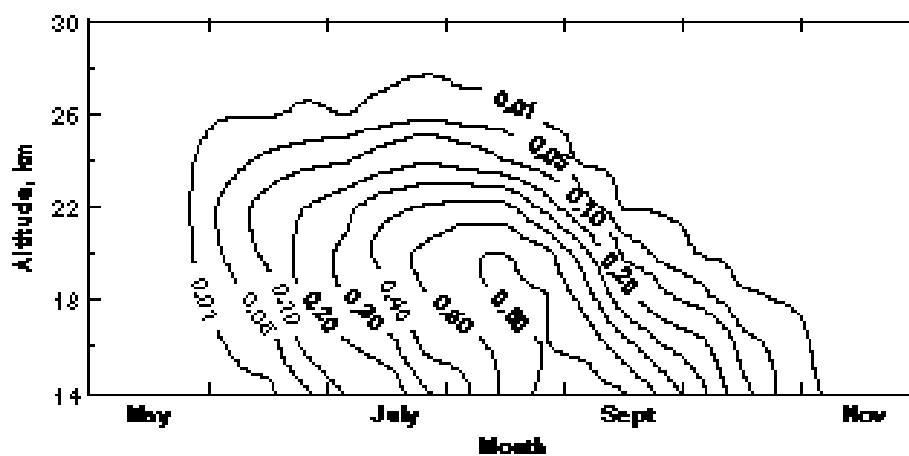


*Figure 2.3.1.2 SAM II zonally averaged Antarctic polar stratospheric cloud (PSC) sighting probabilities for the period from 1979 to 1989.*

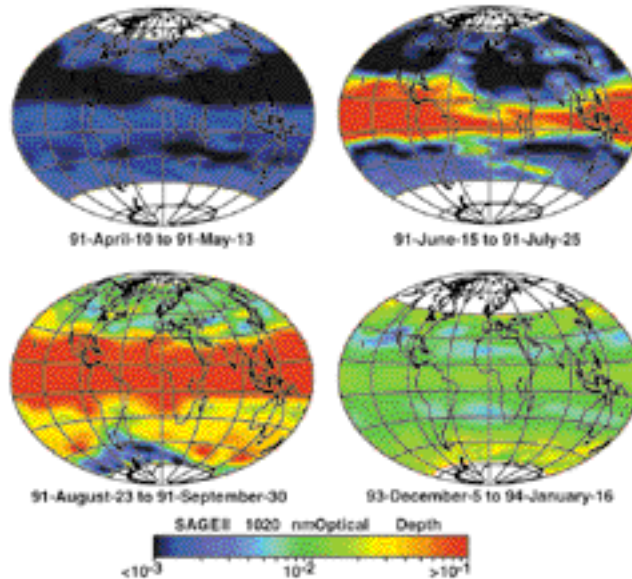


**Figure 2.3.1.3** SAGE II optical depth maps the eruption of Mt. Pinatubo in 1991.

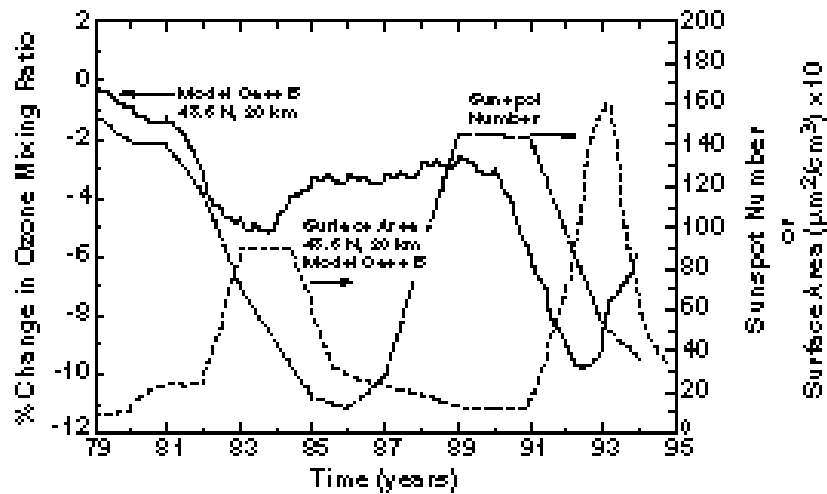


**Figure 2.3.1.4** Calculated ozone depletion at 45 N, 18 km, for Solomon model case B together with the adopted SAGE/SAM aerosol surface area climatology (12-month running means) extrapolated to the future [Solomon et. al.,1996].

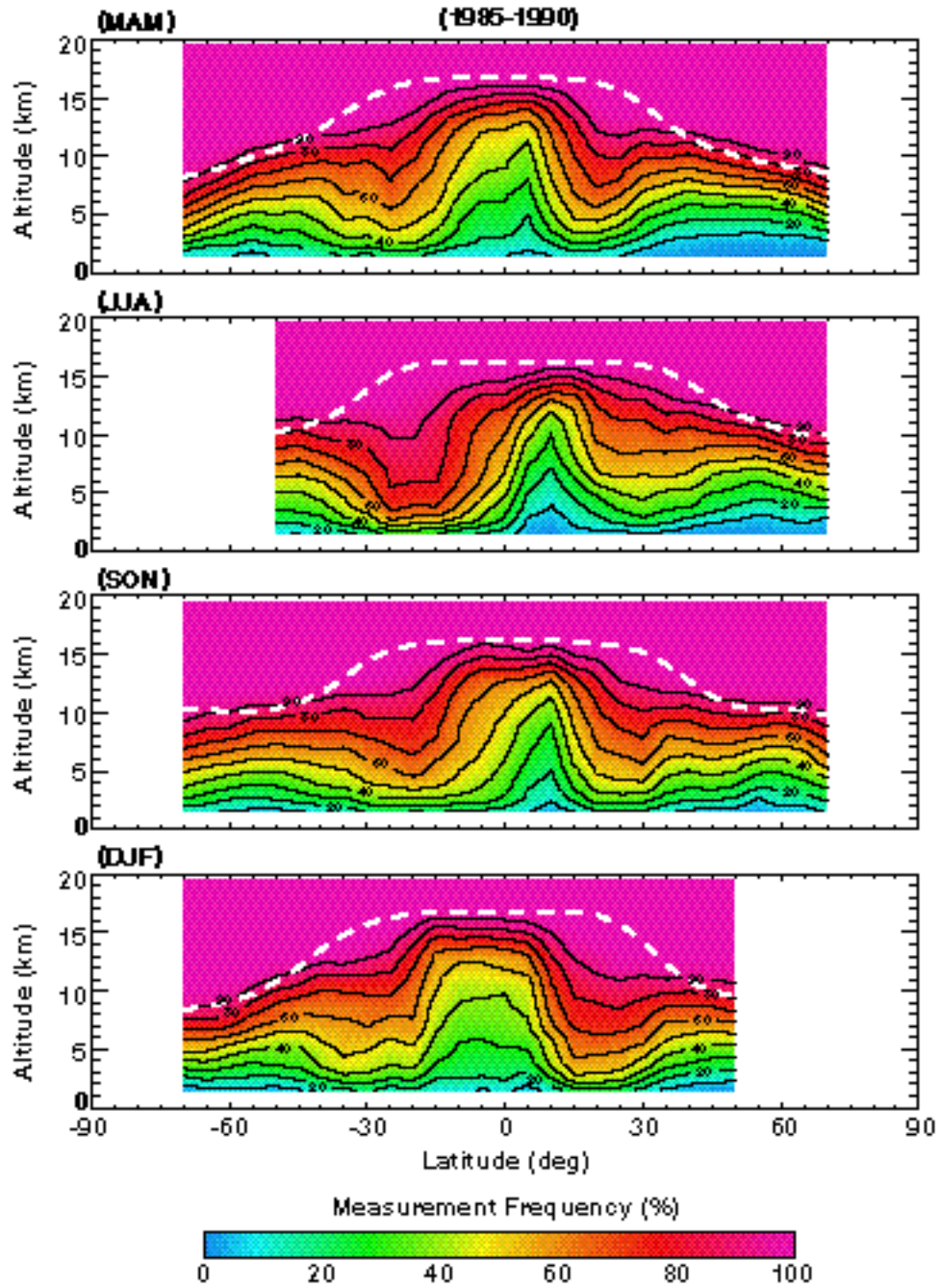


**Figure 2.3.1.5** SAGE II tropospheric measurement frequency (1985-1990) divided into four seasons. The white line denotes the NMC tropopause, and the yellow contour indicates a 50% measurement frequency several kilometers below the tropopause in all seasons and at all latitudes.

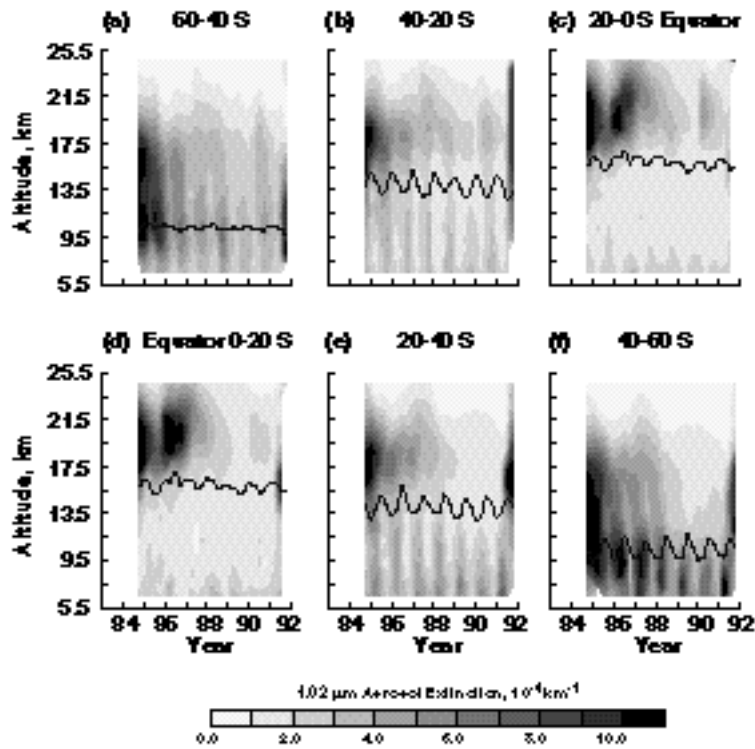


**Figure 2.3.1.6** Zonally averaged SAGE II aerosol extinction measurements in 20 degree zonal bands from 60S to 60N. Note the penetration of stratospheric aerosol into the upper troposphere at high latitudes but not at low latitudes. Also note the upward extending tongues of boundary layer aerosol occurring in each spring.

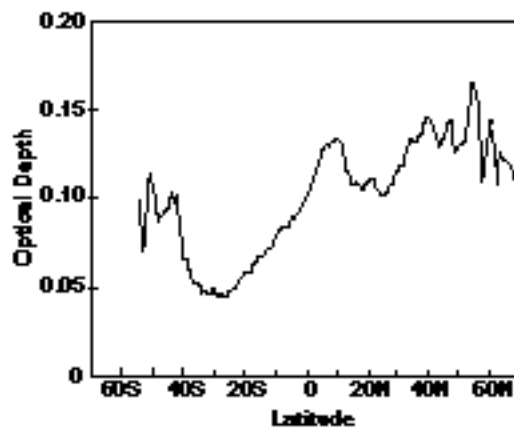


**Figure 2.3.1.7** Zonal average of aerosol optical depth observations from NOAA-7 AVHRR (630 nm wavelength for April 1983).

## 3.0 Algorithm Description

### 3.1 Introduction

#### 3.1.1 Physical Description

SAGE III is designed to measure the attenuation of solar radiation by the Earth's atmosphere due to scattering and absorption by atmospheric constituents during each sunrise and sunset encountered by its spaceborne platform. In addition, SAGE III will make measurements during moonrise and moonset when the atmosphere is not directly illuminated by the Sun. SAGE III consists of three subsystems: the pointing, the imaging, and the spectrometer subsystems. The pointing subsystem consists of a scan mirror which acquires the radiant target (either the Sun or the Moon), and performs vertical scanning (with respect to the Earth's horizon) across the target. A measurement is considered to occur at the point along the line of sight (LOS) from the instrument to the target at which it comes closest to the Earth's surface (i.e., the sub-tangent point). The altitude of that point above the Earth's surface is commonly referred to as the tangent altitude. The imaging subsystem produces a focused image of the target at a focal plane where the "science" aperture, that defines the instrument's instantaneous field of view (IFOV), is situated. The SAGE III IFOV is 30 arcseconds in the vertical direction which translates to approximately 0.5 km at the tangent altitude. The spectrometer subsystem is situated behind the science aperture and consists of an 800-element CCD to measure solar radiation from 280 to 1040 nm with 1 to 2 nm spectral resolution. An additional photodetector is used to measure radiation at 1550 nm.

The viewing geometry of a solar occultation event is illustrated in Figure 3.1.1.1. During an event, the spacecraft motion relative to the Sun's (or Moon's) location permit the measurement of atmospheric transmission at tangent altitudes from the Earth's surface to well above the atmosphere. Since the instrument continually scans vertically across the target, and both the Sun and Moon subtend 32 arcminutes, the transmission at each tangent altitude is measured many times during an event. In addition, by measuring the unattenuated target (along LOS's which do not intersect the Earth's atmosphere) the instrument is recalibrated during each event. Therefore, the instrument provides not only accurate, high vertical resolution measurements of atmospheric transmission, but measurements which are relatively immune to drift in instrument performance.

Figure 3.1.1.2 illustrates the operation of the SAGE III instrument during a typical sunrise event. The two solid lines in the figure represent the upper and lower edges of the Sun as viewed from the spacecraft during the course of the event. The apparent narrowing of the solar image in the lower atmosphere is the result of refraction. The "saw-tooth" line represents the relative motion of the instrument mirror as it scans across the Sun at a nominal rate of 15 arcminutes  $s^{-1}$ . As soon as the instrument acquires the Sun in the lower atmosphere, the initiation of a sunrise event, the IFOV is centered long the radiometric center of the solar image and the scan mirror will move up and down to provide vertical

scanning of a solar disk. The scanning motion continues until the tangent altitude reaches 300 km. Figure 3.1.1.3 shows an example of the measured radiance (expressed in counts) for a SAM II 1000 nm event. The scans are alternately upscans and downscans following solar acquisition. Note the peak intensity of each scan gradually increases until it is constant after approximately 40 s, indicating that the Sun is above the atmosphere. In this example, the attenuation in the lower atmosphere is dominated by Rayleigh and aerosol scattering.

The occultation technique is rather unique in that the measurement coverage, both spatial and temporal, is strongly linked to the orbit parameters of the spacecraft. With one of the prime scientific objectives being the determination and monitoring of trends in atmospheric constituents, SAGE III must be deployed in a fashion which yields adequate spatial (latitudinal) and temporal (seasonal) coverage. The current planned implementation for SAGE III is to place one instrument in a sun-synchronous orbit and another, concurrently, in a mid-inclination orbit. The addition of a second occultation target, the Moon, increases the sampling and offers complementary coverage, for example, the ability to make measurements during the polar winter night where sunrises and sunsets do not occur.

The spectral variation of atmospheric extinction is illustrated in Figure 3.1.1.4 showing the contribution of atmospheric extinction versus wavelength from the different constituents at an altitude of 18 km. Both aerosol and Rayleigh scattering contribute at all wavelengths. Ozone has strong absorption in the Hartley-Huggins band (UV) and the Chappuis band in the visible.  $\text{NO}_2$  absorbs between 350 and 600 nm. Water vapor has absorption lines throughout the visible, but with a strong band near 940 nm.  $\text{NO}_3$  has absorption features between 500 and 650 nm, and  $\text{OCIO}$  has a strong band at 350 nm. SAGE III utilizes the spectrometer with the CCD detector to provide spectral measurements over the wavelength ranges from 280 to 1040 nm so that all of these gaseous species can be detected. An additional channel at 1550 nm is used for near IR aerosol extinction measurements. While SAGE III makes 800 individual spectral measurements, in practice only 70-80 discrete values (combinations of 1 or more digitized CCD element measurements) will be routinely transmitted to the ground. These are sufficient to retrieve all gaseous species and aerosol parameters.



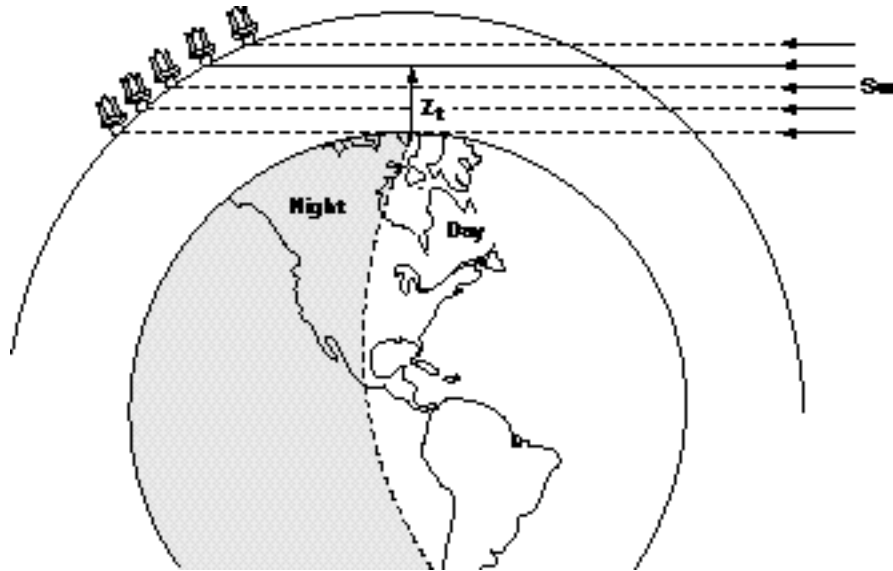


**Figure 3.1.1.1** SAGE III Solar occultation measurement geometry. The tangent altitude is denoted by  $Z_t$ .

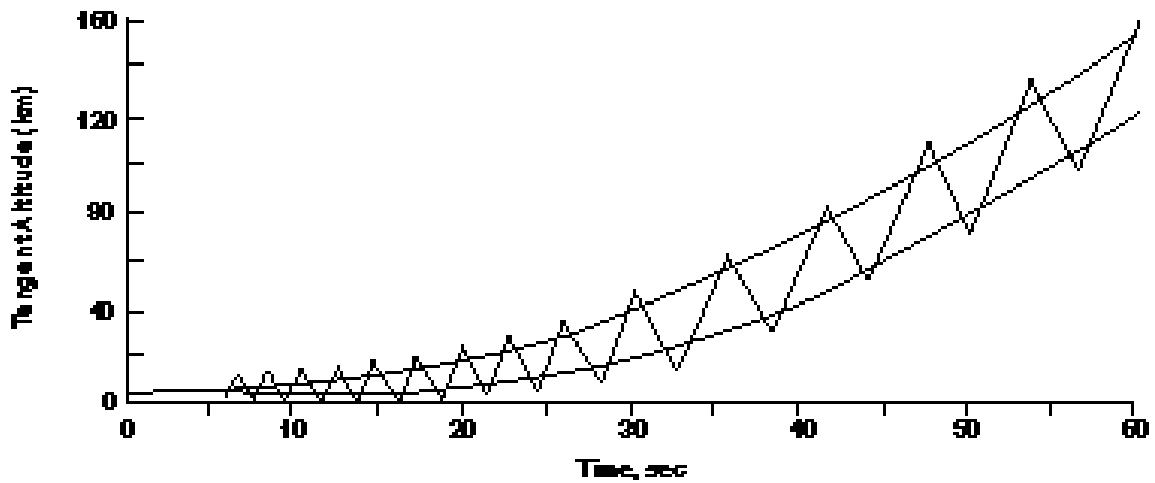


**Figure 3.1.1.2** Typical sunrise event: lines indicate position of top and bottom of the Sun, and scan motion of SAGE scan mirror across the solar disk.

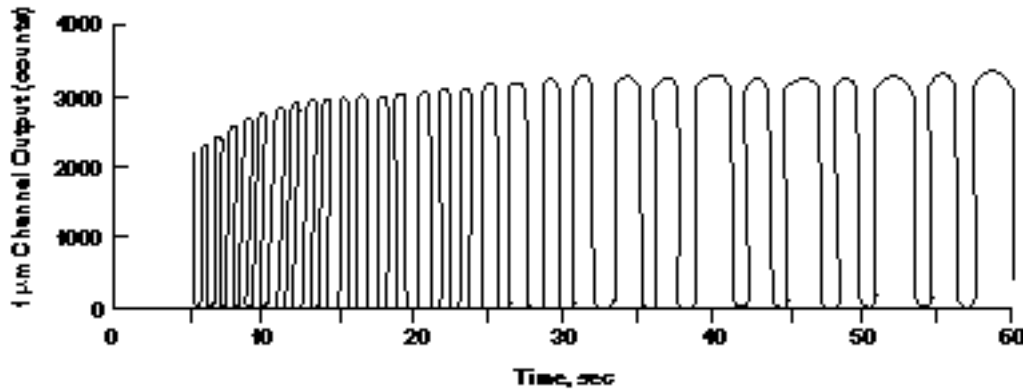


Figure 3.1.1.3 An example of 1 micron extinction from SAM II during a sunrise event.

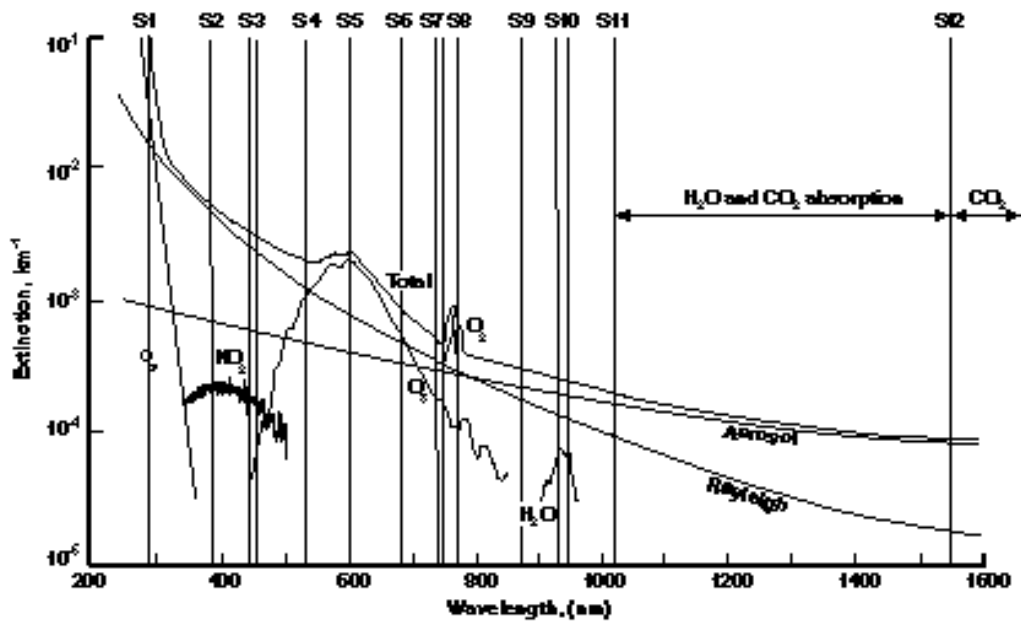


Figure 3.1.1.4 Wavelength dependence of atmospheric extinction at 18 km ( $\text{NO}_3$  and  $\text{OClO}$  are not shown).

### 3.1.2 The Forward Problem

The equation of radiative transfer in one dimension for radiance,  $I(\lambda, x)$ , at wavelength  $\lambda$ , at an arbitrary point  $x$  is given by

$$\frac{dI(\lambda, x)}{d(\lambda, x)} = S(\lambda, x) - I(\lambda, x), \quad (3.1.2.1)$$

where  $S$  is the source function and  $d(\lambda, x)$  is the optical depth between points  $x$  and  $x+dx$ . The optical depth per unit distance ( $d(\lambda, x)/dx$ ) is commonly referred to as extinction. The source function consists of contributions from both single and multiple scattering as well as emission. For SAGE III measurements, wavelengths, and geometry

(directly observing the Sun through a small IFOV), scattering and emission terms are very small relative to the directly transmitted component and can be ignored. Therefore, Equation 3.1.2.1 can be simplified to

$$\frac{dI(\lambda, x)}{dx} = -I(\lambda, x). \quad (3.1.2.2)$$

The solution to this equation, when the unattenuated radiance (at  $x=0$ ) is given by  $I(\lambda, 0)$ , is given by

$$I(\lambda, x) = I(\lambda, 0)e^{-\tau(\lambda, x)}. \quad (3.1.2.3)$$

Then, the irradiance,  $R_N$  as measured by SAGE III for channel “N”, can be expressed as

$$R_N(Z_t) = \int_0^\infty \int_{-\theta/2}^{\theta/2} I(\lambda, 0)e^{-\tau(\lambda, Z_t)} W(\lambda) d\lambda d\theta, \quad (3.1.2.4)$$

where  $\tau(\lambda, Z_t)$  is the optical depth along the line of sight at tangent height  $Z_t$  between the instrument and the Sun,  $\Delta\lambda$  is the spectral width of channel N with band pass function  $W(\lambda)$ ,  $\theta$  is the angular field of view of the instrument with response  $W(\theta)$ . The value of  $\tau(\lambda, Z_t)$  varies with tangent altitude; it is effectively 0 above 100km and generally increases downward. It is composed of contributions from Rayleigh, aerosol, and gaseous species extinction. Transmission along the line of sight,  $T_N(Z_t)$  (also called the slant path transmission), at tangent height  $Z_t$ , is defined as

$$T_N(Z_t) = R_N(Z_t) / R_N(Z_t^*), \quad (3.1.2.5)$$

where  $(Z_t^*)$  is a tangent altitude well above the atmosphere ( $> 100$  km).

## 3.2 Retrieval Algorithm Description

### 3.2.1 Overview and Assumptions

In as much as SAGE III is a fourth generation instrument, the operational software also represents a fourth level in the complexity of the species separation algorithm. The earliest instrument, the Stratospheric Aerosol Measurement (SAM II) (1978-1994) was a single channel (or wavelength) instrument where external Rayleigh or molecular scattering effects were subtracted from the line of sight optical depths. Subsequently, the remaining optical depth peeled to a vertical profile of aerosol extinction at 1000 nm. The first Stratospheric Aerosol and Gas Experiment (SAGE) (1979-1981), and its follow-on mission SAGE II (1984-present), used measurements (often referred to as “channels”) of atmospheric line-of-sight transmission at multiple wavelengths (four and seven, respectively) from the ultraviolet to the near-infrared. These extra channels were employed to infer vertical profiles of multi-wavelength aerosol extinction, ozone ( $O_3$ ), nitrogen dioxide ( $NO_2$ ), and,

in the case of SAGE II, water vapor ( $\text{H}_2\text{O}$ ). These instruments also introduced a new challenge: separating the effects of different species when they affect transmission at more than one measurement wavelength [Chu et al., 1989]. While these experiments were highly successful, the extent of mutual interference limited the vertical domain and the accuracy of each species retrieved.

For solar occultation events, SAGE III uses 87 channels between 290 and 1540 nm at which vertical profiles of transmission are determined. This data is used to produce profiles of the molecular density of  $\text{O}_3$ ,  $\text{NO}_2$ ,  $\text{H}_2\text{O}$ , aerosol extinction at 9 wavelengths, cloud presence, temperature, and pressure. With this in the spectral density of the channels, the inversion algorithm has been designed to minimize past difficulties with species separation and improve both the accuracy and vertical range of the data products. In addition, it adds new aerosol extinction channels (up to 9 wavelengths), formalizes cloud presence as a data product, and temperature and pressure profiling through the use of the oxygen A Band located near 765 nm. The process or algorithm that leads from raw instrument counts to data products can be broken into two distinct parts: the transmission algorithm and the species inversion algorithm. The different steps in the transmission and inversion algorithms and the overall flow of the algorithm are illustrated in Figure 3.2.1.1. Details of the transmission algorithm may be found in the SAGE III Transmission ATBD (LaRC475-00-108). A brief overview of the transmission algorithm follows. The species-inversion algorithm overview is discussed in Section 3.2.2. The species-specific segments of the algorithm are found in 3.2.3.

### ***Transmission Algorithm Summary***

The function of the transmission algorithm is to produce multi-wavelength slant path transmission profiles from time sequences of radiometric and engineering measurements by the SAGE III instrument. As shown in Figure 3.2.1.1, this process can be separated into five components: data screening, position registration, altitude registration, wavelength registration, and data grouping and statistics. The first step in the transmission algorithm is the screening of the input level zero (telemetry) data. The data-screening algorithm locates missing or bad data and determines whether the data are recoverable. Next, the position registration algorithm determines solar point positioning and the tangent height. The tangent height is the altitude at which the ray is closest to the Earth's surface for the line-of-sight that originates from the center of the instrument's field of view to the position on the sun. Taking the ratio of the science scan data (any data with an associated tangent height below 100 km) relative to the same solar position on exo-atmospheric scans produces atmospheric transmission for an individual measurement. The tangent height calculation provides the height registration of the derived transmission values. Generally, tangent height is dominated by geometric concerns, however it is corrected for atmospheric refraction, which becomes increasingly significant below 30 km. Each channel is also calibrated for wavelength using an operation mode of the instrument that occurs at tangent altitudes well above normal operation regions in the atmosphere. Using all 800 pixels, a multi-linear

regression procedure is used to assign spectral positions to individual pixels by using a standard solar spectrum. The solar spectrum has complex spectral features including the solar Fraunhofer lines that measured by the SAGE III CCD spectrometer system. In this manner, shifting and stretching of the pixels on the CCD device due to thermal or mechanical perturbations can be accounted for and the center wavelength for each of the 800 pixels will be accurately determined. The final step in the transmission algorithm is the data grouping and statistics. This procedure takes the individual transmission data (up to several thousand data points per channel) into altitude profiles and performs statistical analyses to determine the characteristics of the distribution of the measured data in each group. Transmission profiles for each channel are produced on a 0.5-km grid from 0.5 km to 100 km with an uncertainty estimate. The correlation between channels at 521, 1020 and 1540 nm at altitudes between 6.5 and 26.5 km is also calculated as required input to the cloud presence algorithm.

### 3.2.2 Species Separation Algorithm

The species separation algorithm involves the inversion of the multi-wavelength slant path transmission profiles into vertical profiles of the molecular density of SAGE III-measured gas species as well as aerosol extinction at several wavelengths between 290 nm and 1550 nm. For most species, rather than work directly from transmission profiles  $T(z_t)$ , the inversion algorithm works with the slant path optical depth,  $\tau(z_t)$ , which can be expressed for wavelength,  $\lambda$ , and slant path tangent height,  $z_t$ , as

$$\tau(z_t) = -\ln(T(z_t)). \quad (3.2.2.1)$$

The slant path optical depth at each SAGE III measurement wavelength consists of several components including molecular or Rayleigh scattering, aerosol extinction, and usually absorption by one or more gaseous species. At each tangent height, SAGE III will make measurements at 87 wavelengths (or channels) between 290 nm and 1540 nm distributed as shown in Table 3.2.2.1. The ensemble of SAGE III measurements at a given tangent height can be expressed a series of linear equations of the form

$$\tau = \tau_R + \tau_a + \sum_{n=1}^N \tau_{gn}, \quad (3.2.2.2)$$

where  $\tau_R$  is the Rayleigh slant path optical depth,  $\tau_a$  is the aerosol slant path optical depth, and  $\tau_{gn}$  is the slant path optical depth for gas species  $n$ , where  $N$  can be from 0 to 4. A crucial element of the inversion process is the partitioning of the total slant path optical depth at each wavelength and tangent altitude into the contributions of the individual components. Thus, for the measurement ensemble, there are unknown molecular and aerosol components at each wavelength, unknown temperature and pressure, as well as unknown ozone, nitrogen dioxide, and water vapor molecular densities, or, in a nominal sense, more than twice as many unknown parameters as measurements at each tangent altitude. Table 3.2.2.1 lists the primary and interfering species for each channel.

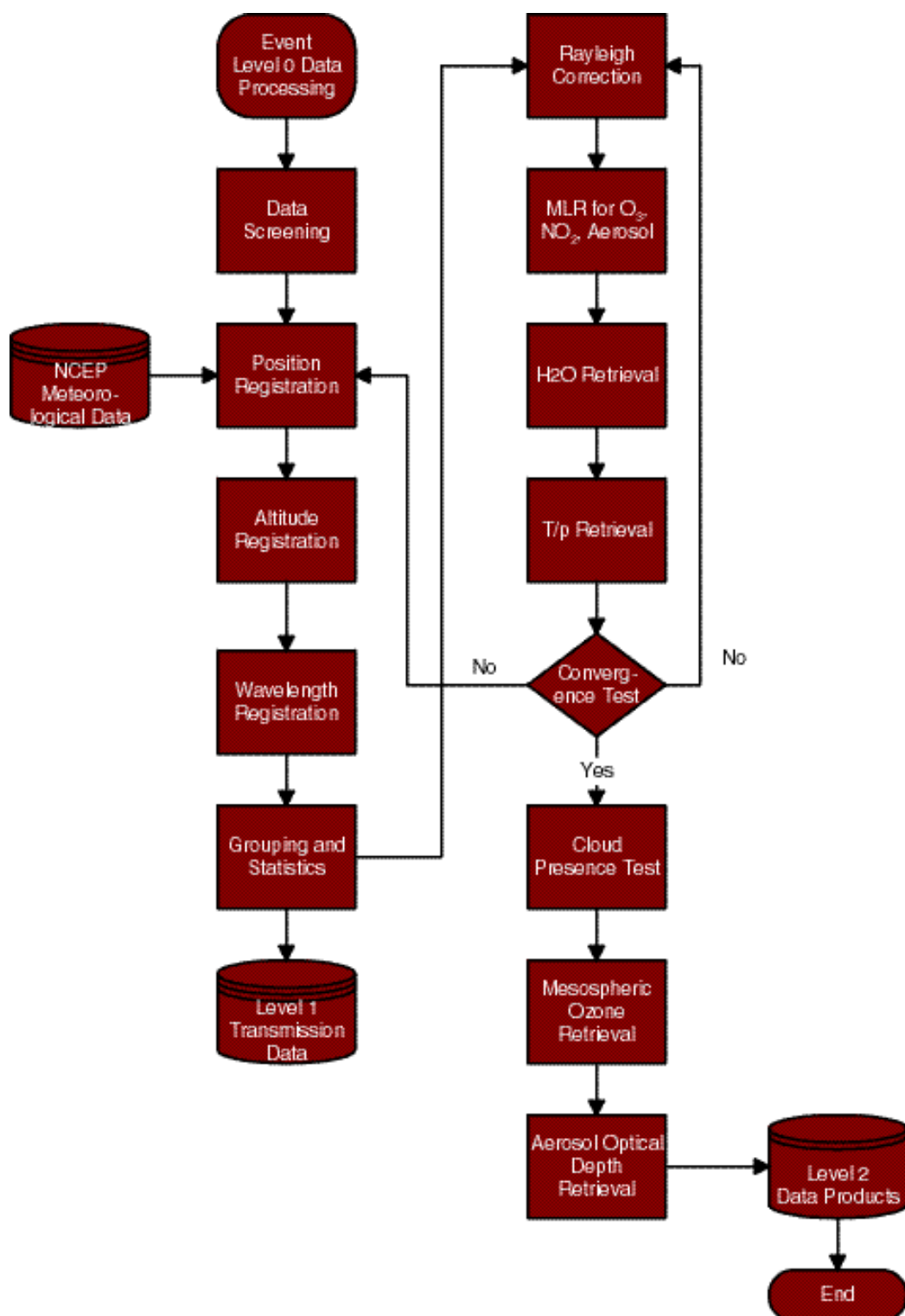


**Figure 3.2.1.1** Flow of data through the SAGE III processing algorithm.

**Table 3.2.2.1 SAGE III Channel Groupings with Primary and Interfering Species.**

Channel Grouping		Primary Species	Interfering Species+
S1	290 nm	O <sub>3</sub>	
S2	385 nm	Aerosol	NO <sub>2</sub> , O <sub>3</sub>
S3	433-450 nm	NO <sub>2</sub> , Aerosol	O <sub>3</sub>
S4	521 nm	Aerosol, Cloud	NO <sub>2</sub> , O <sub>3</sub>
S5	563-622 nm	O <sub>3</sub> , Aerosol	NO <sub>2</sub> , H <sub>2</sub> O
S6	676 nm	Aerosol	O <sub>3</sub>
S7	758 nm	Aerosol	O <sub>3</sub>
S8	759-771 nm	O <sub>2</sub> (T,P)	O <sub>3</sub>
S9	869 nm	Aerosol	O <sub>3</sub> , H <sub>2</sub> O
S10	933-960 nm	H <sub>2</sub> O	O <sub>3</sub>
S11	1020 nm	Aerosol, Cloud	O <sub>3</sub>
S12	1540 nm	Aerosol, Cloud	CO <sub>2</sub> , H <sub>2</sub> O

+ Any species influencing the retrieval of the primary species except the omnipresent Rayleigh and aerosol components.

The Rayleigh contribution has a well-known wavelength dependence ( $\lambda^{-4}$ ) and is dependent only on the total molecular mass along the slant path. Formally, this can be expressed as

$$R = \int_{z_f}^z \rho(z) dx(z, z_f), \quad (3.2.2.3)$$

where  $R$  is the Rayleigh mass extinction coefficient determined using the formulation of Bucholz (1996). And  $\rho(z)$  is the molecular mass density as a function of height and determined from the current values for the temperature and pressure profiles and the ideal gas law, and  $dx(z, z_f)$  is the length of the slant path between the altitudes of  $z$  and  $z+dz$  and includes the effects of spherical geometry and wavelength-dependent refraction [Chu, 1983]. Like the refraction component of the transmission algorithm, the unknown Rayleigh slant path optical depth is initially estimated using temperature and pressure profiles supplied by the NCEP and the GRAM 95 climatology (for altitudes above 50 km). A branch back to either refraction module or the Rayleigh calculation may be required if the temperature and pressure product is the difference between the final product and the initial guess is sufficiently large.

The next step in the inversion process is to derive slant path number density profiles for  $\text{NO}_2$  and  $\text{O}_3$  using multiple linear regression (MLR) and the channels for these species listed in Table 3.2.2.1 (S3 and S5). The advantage of this procedure is that the fine structure of these species, particularly  $\text{NO}_2$ , in these bands permits the extraction of the column densities independently of either the aerosol or molecular components. It is necessary to simultaneously solve for these species since they absorb significantly in both spectral regions (433-450 nm and 562-622 nm). The MLR inversion process is discussed in detail in Section 3.2.3 of the  $\text{NO}_2$ ,  $\text{NO}_3$ ,  $\text{OCIO}$ , and  $\text{O}_3$  ATBDs (LaRC475-00-101, LaRC475-00-102, LaRC475-00-103, LaRC475-00-107, respectively). Once the slant-path column densities have been derived, the influence of  $\text{NO}_2$  and  $\text{O}_3$  is removed from all measurement wavelengths in which it is a component excluding the mesospheric ozone channel at 290 nm. The slant path aerosol optical depths for the nominal SAGE III aerosol channels at 385, 448, 521, 595, 676, 758, 869, 1020, and 1540 nm (involving S2-S7, S9, S11 and S12). They are retrieved as residuals of the MLR retrievals of  $\text{O}_3$  and  $\text{NO}_2$  and thus are effectively a part of the MLR procedure.

In both the center of the ozone Chappuis band and in some of the aerosol channels, water vapor is a minor contributor that cannot be initially corrected. Thus, in the first iteration, the water vapor correction in these channels will be neglected. While, for subsequent iterations, it will be determined using the current retrieved water vapor profile using the method described in Section 3.2.3 of the SAGE III Water Vapor ATBD (LaRC475-00-100).

The next stage in the retrieval process is the retrieval of the water vapor profile. Since both aerosol and ozone significantly contribute in the SAGE III water vapor channels between 933 and 960 nm (Table 3.2.2.1), the first step in the water vapor retrieval algorithm is to isolate the water vapor contribution. The effects of ozone can be estimated using the MLR ozone product and the appropriate cross sections. For aerosols, we have initially implemented a simple multi-channel interpolation to remove the influence of aerosol using the aerosol derived as a part of the MLR procedure. This is similar to the approach used with earlier SAGE inversions however, the increase in number and proximity of aerosol channels greatly improve this approach and modeling indicates that this is sufficient for most circumstances. However, more robust approaches are under investigation that allow the retrieval to estimate both the water vapor profile, aerosol, and ozone effects independently of estimates of aerosol and ozone based on measurements at other wavelengths. This may be particularly advantageous for ozone effects since the temperature dependence of ozone absorption in the water vapor feature is not well known and the magnitude of ozone absorption may exceed that of water vapor at some altitudes. With the current method, given the profile of water vapor slant path optical depths, the vertical profile of water vapor density is solved for using the procedure described in Section 3.2.3 of the SAGE III Water Vapor ATBD (LaRC475-00-100). It is a standard Levenberg-Marquardt inversion that, unlike aerosol,  $\text{O}_3$ , and  $\text{NO}_2$  (which remain in slant path format at this point of the inversion process), directly produces a vertical profile of water vapor



molecular density. The derived water vapor profile may be used on subsequent iterations to remove the influence of water outside the nominal water vapor band. In particular, water vapor absorbs weakly near 600 nm (and thus influences ozone retrievals) as well as at 869 nm (influencing the aerosol extinction measurement at that wavelength).

The next stage in the retrieval process is the retrieval of temperature and pressure (T/p). Like water vapor, aerosol and ozone contribute in a generally small but significant way to the total optical depth in the SAGE III O<sub>2</sub> A-Band channels between 759 and 771 nm (Table 3.2.2.1). As for the water vapor retrieval, we have initially implemented a simple multi-channel interpolation to remove the influence of aerosol using the aerosol slant path optical depth derived as a part of the MLR procedure. In addition, again, the effects of ozone can be estimated using the MLR ozone product and the appropriate cross sections. Once those species have been accounted for, the residual values are the slant path oxygen A-band optical depths. Given the profile of oxygen A-band slant path optical depths (at 14 channels), the vertical profiles of temperature and pressure are determined using a non-linear Marquardt-Levenberg method described in Section 3.2.3 of the SAGE III Temperature & Pressure ATBD (LaRC475-00-104). Like the water vapor inversion algorithm, the T/p procedure yields vertical profiles rather than slant path profiles.

Both the water vapor and the temperature and pressure retrieval algorithms require a forward model as part of the retrieval process. We have implemented the Emissivity Curve-of-Growth Approximation (EGA). Testing suggests that it is adequate and far quicker than line-by-line calculations.

At this point of the retrieval process, it is possible that branching backward in the retrieval process is possible. While unlikely, it is possible that the change in atmospheric density (as inferred by the T/p retrieval) to be sufficiently large to change altitude registration performed in the transmission section of the retrieval process. In this case, the processing branches back to the refraction computation segment of the transmission calculation. It is also possible that the processing could branch back to the Rayleigh optical depth or water vapor sections of the species separation algorithm if the change in the estimated Rayleigh correction profile exceeds the estimated uncertainty in those profiles. Otherwise, the processing branches to the final stages of the inversion process. The branching process will be run-time controllable feature.

The final stages of the retrieval algorithm are mesospheric ozone retrieval, profile peeling, cloud presence detection, and aerosol stratospheric optical depth calculation. The mesospheric ozone algorithm makes use of the 290 and 385 nm line-of-sight optical depths (uncorrected for Rayleigh). This is a straightforward algorithm and discussed in the SAGE III Ozone ATBD (LaRC475-00-107). Profile peeling (the conversion from line-of-sight or slant path optical depth to extinction profile or number density) follows the SAGE II processing method in which a modified-Chahine method [Chahine; 1972, Twomey, 1975.

Chu and McCormick, 1979; Chu, 1985; Chu *et al.*, 1989] was employed, though alternative methods are available as runtime options including simple onion peeling.

The Cloud Presence Algorithm is detailed in SAGE III Cloud ATDB (LaRC475-00-106) and makes use of aerosol extinction at 521, 1020, and 1540 nm between 6.5 and 26.5 km. The basic algorithm relies upon wavelength ratios between these aerosol extinction in these channels (clouds tend to be “white”) but also requires a separate user driven quality control process for which a separate document is being developed.

With all species transformed to vertical profiles, construction of the data products listed in Table 1.2.1 is executed and the data made available for archival.

### ***Uncertainty Estimation***

Satellite measurements contain uncertainty that includes both random and systematic components. As in the SAGE and SAGE II retrievals, the SAGE III measurements will provide uncertainty estimates for random components [Russell *et. al.*, 1981; Chu *et. al.*, 1993]. In the case of systematic uncertainty, it is normally secondary and can be assessed through sensitivity analysis. There are three primary sources of the random component of the uncertainty (a) line-of-sight optical depth measurement errors, (b) the Rayleigh optical depth estimate, and (c) uncertainties resulting from the removal of contributions by interfering species. The basic concept of the reported SAGE III data-products uncertainties is the transference of measurement error to data product error via the mathematical processes that produce them.

The grouping and statistics algorithm described in the SAGE III Transmission ATDB determines errors in the line-of-sight optical depth (or its companion transmission). The measurement error can be modified by the removal or clearing of the species which are considered to “interfere” with the retrieval process. This usually includes the Rayleigh component and, in some cases, one or more data products such as the removal of ozone from the water vapor and temperature/pressure channels. If branching back occurs, the Rayleigh uncertainty would be modified and water vapor uncertainty included at the appropriate channels. This modified error then becomes the base measurement error.

The method by which these uncertainties propagate into species is greatly dependent on method employed. For instance, MLR error in the line-of-sight values is a product of the MLR mathematical process measurement spectrum and not strongly dependent on the estimated signal error. This is described in more detail in the O<sub>3</sub>, NO<sub>2</sub>, NO<sub>3</sub>, and OCIO ATBDs and in common reference material [e.g., Bevington, 1969]. Since aerosol is predominately a residual of the MLR process its error is dominated by the measurement error and the species errors estimated by this algorithm.

To propagate errors determined for line-of-sight quantities ( $O_3$ ,  $NO_2$ ,  $NO_3$ ,  $OCIO$ , and aerosol) to the uncertainties in the vertical profile is a straightforward application of the least-squares form of onion peeling. The vertical profile of measurement variance ( $a$  vector,  $q$ ) (uncertainty squared) is multiplied by the inverse of the path length matrix,  $P$  to produce the data product variance which can be expressed as

$$\underline{g} = P^{-1} \underline{q}$$

An element of the limb path length matrix contains the physical distance traversed by the line-of-sight ray path for a tangent layer  $n$  through layer  $m$  (non-zero only for  $m \geq n$ ).

In the Marquardt-Levenberg method, (used by water vapor and T/p retrieval algorithms), covariance matrices are produced that translate measurement error into species uncertainties. In this case, since the products of these algorithms are the final data products no further modification of the estimated error is required.

**Table 3.2.2.2 Uncertainty Estimates**

Species	Expected Precision	Altitude Range
Aerosol 1020 nm, 521 nm	5%	0-40
Temperature	2 K	0-85
Pressure	2%	0-85
Ozone (Solar)	10%	6-85
Ozone (Lunar)	<10%	16-35
Nitrogen Dioxide (Solar)	15%	10-50
Nitrogen Dioxide (Lunar)	<10% <15%	22-32 19-37
Water Vapor	<5% 5%-15%	<33 33-42
Chlorine Dioxide	25%	15-25
Nitrogen Trioxide	10%	10-50

Note that systematic sources of error are neglected in discussion above. These arise primarily due to the degree to which basic physical assumptions are obeyed (e.g., spherical homogeneity; see Appendix C), imperfect knowledge of instrument performance, spacecraft ephemeris, and spectroscopy. An assessment of the current state of spectroscopy as it relates to SAGE III is given in Appendix D.

### 3.2.3 Aerosol Retrieval

Aerosol slant path optical depth is retrieved as a residual of the MLR retrievals of O<sub>3</sub> and NO<sub>2</sub> and thus is effectively a part of the MLR procedure. If the algorithm branches back and water vapor data is available, some channels are corrected for water vapor particularly at 869 and 1540 nm (which is also cleared for absorption by carbon dioxide). The uncertainty in the slant path aerosol values,  $\tau_{aer}$ , is calculated based on measurement error,  $\tau_m$ , and errors associated with the removal of interfering species,  $\tau_{species}$ , or

$$\tau_{aer}^2 = \tau_m^2 + \tau_{species}^2$$

For all nine channels this includes at least Rayleigh but also generally includes the effects of at least one other species including O<sub>3</sub>, NO<sub>2</sub>, H<sub>2</sub>O, and CO<sub>2</sub> (which is estimated from the temperature and pressure profile for the 1540 nm channel).

Aerosol slant path optical depth estimates in the temperature and pressure channels (S8) and water vapor channels (S10) are accomplished using Lagrangian interpolation (e.g., Stark, 1970) using nearby aerosol channels. This method, when tested against methods compared to more physically based methods yields similar results. Current research on both the temperature pressure retrieval and the water vapor retrieval will ultimately make this function unnecessary.

### 3.3 Algorithm Testing Requirements

Algorithm testing will be performed both prior to launch and during the lifetime of the instrument using the SAGE III data simulator. The data simulator models both a ray tracing-based model of the atmosphere and accounts for measured and modeled instrument performance. For instance, the instrument model includes the effects of uncertainties in the instrument wavelength-band pass, fields of view, detector response, and spacecraft telemetry. The atmospheric model can include realistic uncertainties in errors in external data sets (e.g., molecular spectroscopy and lunar albedo) and the effects of atmospheric spatial inhomogeneity. The simulator should (and has) helped us to identify software errors and below standard performance in individual retrieval components. The simulator is maintained under configuration control and is considered an adjunct component of the primary operational software.

### 3.4 Validation Plan

Planning for the validation of all SAGE III data products is covered in the SAGE III Validation Plan (LARC475-00-020). Validation plans are uncertain due to the slip in SAGE III/Meteor-3M launch date and that document will be revised as launch date and available funds available for validation become more certain.

### **3.5 Quality Control and Diagnostics**

Routine processing will generate a series of quality indicators that assess the quality of the data products and the degree to which the processing of each event was completed according to expectation. The details of this process are outlined in The SAGE III Data Management System Quality Assurance Document (LaRC475-03-115).

#### 4.0 References

- d'Almeida, G. A., P. Koepke, and E. P. Shettle, *Atmospheric aerosols, global climatology and radiative characteristics*, A. Deepak Publishing, 1991.
- Bandeem, W. R., and R. S. Fraser, *Radiative effects of the El Chichon Volcanic eruption: Preliminary results concerning remote sensing*, NASA TM 84959, 1982.
- Bates, T., and J. Gras, Eds., *Southern Hemisphere Marine Aerosol Characterization Experiment (ACE-1)*, NOAA/PMEL, Seattle, 1994.
- Brogniez, C., and J. Lenoble, Size distribution of stratospheric aerosol from SAGE II multi-wavelength extinctions. *Aerosols and Climate*, P. V. Hobbs and M. P. McCormick, Editors, A. Deepak Publishing, 305-311, 1988.
- Buglia, J. J., *Effects of ephemeris errors on the accuracy of the computation of the tangent point altitude of a solar scanning ray as measured by the SAGE I-II instrument*, NASA TP-2866, 1989.
- Chahine, M. T., A general relaxation method for inverse solution of the full radiative transfer equation, *J. Atmos. Sci.*, 29, 741-747, 1972.
- Charlson, R. J., and J. Heintzenberg, *Aerosol Forcing of Climate*, Wiley, New York, 416 pp., 1995.
- Chin, M., and D. D. Davis, A reanalysis of carbonyl sulfide as a source of stratospheric background aerosol, *J. Geophys. Res.*, 8993-9005, 1995.
- Chu, W., and M. P. McCormick, Inversion of stratospheric aerosol and gaseous constituents from spacecraft solar extinction data in the 0.38-1.0 micron wavelength region, *Appl. Opt.*, 18, 1404-1414, 1979.
- Chu, W. Calculation of atmospheric refraction for space craft remote sensing applications, *Appl. Opt.*, 22, 721-726, 1983.
- Chu, W. P., Convergence of Chahine's nonlinear relaxation inversion method used for limb viewing remote sensing, *Appl. Opt.*, 24, 445-447, 1985.
- Chu, W. P., M. P. McCormick, J. Lenoble, C. Brogniez, and P. Pruvost, SAGE II inversion algorithm, *J. Geophys. Res.*, 94, 8339-8351, 1989.
- Chu, W. P., E. W. Chiou, J. C. Larsen, L. W. Thomason, D. Rind, J. J. Buglia, S. Oltmans, M. P. McCormick, and L. M. McMaster, Algorithms and sensitivity analyses for Stratospheric Aerosol and Gas Experiment II water vapor retrieval, *J. Geophys. Res.*, 98, 4857-4866, 1993.
- Crutzen, P. J., The possible importance of OCS for the sulfate layer of the stratosphere. *Geophys. Res. Lett.*, 3, 73-76, 1976.

- Cunnold, D. M., W. P. Chu, R. A. Barnes, M. P. McCormick, and R. E. Veiga, Validation of SAGE II ozone measurements, *J. Geophys. Res.*, 94, 8339-8352, 1989.
- Deshler, T., D. J. Hofmann, B. J. Johnson, and W. R. Rozier, Balloonborne measurements of the Pinatubo aerosol size distribution and volatility at Laramie, Wyoming during the summer of 1991. *Geophys. Res. Lett.*, 19, 199-202, 1992.
- Deshler, T., B. J. Johnson, and W. R. Rozier, Balloonborne measurements of Pinatubo aerosol during 1991 and 1992 at 41 N: vertical profiles, size distribution, and volatility. *Geophys. Res. Lett.*, 20, 1435-1438, 1993.
- Diner, D. J., C. J. Bruegge, J. V. Martonchik, T. P. Ackerman, R. Davies, S. A. W. Gerstl, H. R. Gordon, P. J. Sellers, J. Clark, J. A. Daniels, E. D. Danielson, V. G. Duval, K. P. Klaasen, G. W. Lilienthal, D. I. Nakamoto, R. J. Pagano, and T. H. Reilly, MISR: A Multiangle Imaging Spectro-Radiometer for Geophysical and Climatological Research from EOS, *IEEE Trans. Geosci. Rem. Sens.* 27, 200-214, 1989.
- Durkee, P. A., F. Pfeil, E. Frost, and R. Shema, Global analysis of aerosol particle characteristics, *Atmosph. Env.* 25A, 2457-2471, 1991.
- Dutton, E. G., and J. R. Christy, Solar radiative forcing at selected locations and evidence for global lower tropospheric cooling following the eruptions of El Chichon and Pinatubo, *Geophys. Res. Lett.*, 19, 2313-2316, 1992.
- Fiocco, G., D. Fua, and G. Visconti (Eds.), *The Effects of Mt. Pinatubo Eruption on the Atmosphere and Climate*, NATO ASI Series Volume, Subseries I, "Global Environmental Change," Springer-Verlag, 1996.
- Gleason, J. F., P. K. Bhartia, J. R. Herman, R. McPeters, P. Newman, R. S. Stolarski, L. Flynn, G. Labow, D. Larko, C. Seftor, C. Wellemeyer, W. D. Komhyr, A. J. Miller, and W. Planet, Record low global ozone in 1992, *Science*, 260, 523-526, 1993.
- Grainger, R. G., A. Lambert, F. W. Taylor, J. J. Remedios, C. D. Rodgers, M. Corney, and B. J. Kerridge, Infrared absorption by volcanic stratospheric aerosols observed by ISAMS, *Geophys. Res. Lett.*, 20, 1283-1286, 1993.
- Griggs, M., Measurement of atmospheric aerosol optical thickness over water using ERTS-1 Data, *J. Air Pollut. Control Ass.*, 25, 622-626, 1975.
- Hansen, J., D. Johnson, A. Lacis, S. Lebedeff, P. Lee, D. Rind, and G. Russell, Climate impact of increasing atmospheric carbon dioxide, *Science*, 213, 957, 1981.
- Hansen, J. E., A. Lacis, R. Ruedy, M. Sato, and H. Wilson, How sensitive is the world's climate?, *Nat. Geog. Res. Explor.* 9, 142-158, 1993.
- Hansen, J. et al., A Pinatubo climate modeling investigation, in *Fiocco et al., Op. cit.*, 1995
- Hervig, M. E., J. M. Russell III, L. R. Gordley, J. H. Park, and S. R. Drayson, Observations of aerosol by the HALOE experiment onboard UARS: A preliminary validation. *Geophys. Res. Lett.*, 20, 1291-1294, 1993.

- Hobbs, P. V., ed. A Plan for an International Global Aerosol Program (IGAP). Available from Department of Atmospheric Sciences, University of Washington, Seattle, WA 98195, USA, 1994.
- Hofmann, D. J., Increase in the stratospheric background sulfuric acid aerosol mass in the past 10 years, *Science*, 248, 996-1000, 1990.
- Hofmann, D. J., Aircraft sulfur emissions. *Nature*, 349, 659, 1991.
- Hofmann, D. J., S. J. Oltmans, J. A. Lathrop, J. M. Harris, and H. Vomel, Record low ozone at the South Pole in the spring of 1993, *Geophys. Res. Lett.*, 21, 421-424, 1994.
- Hofmann, D. J., S. J. Oltmans, J. M. Harris, J. A. Lathrop, G. L. Koenig, et al., Recovery of stratospheric ozone over the United States in the winter of 1993-1994, *Geophys. Res. Lett.*, 21, 1779-1782, 1994.
- Holben, B., E. Vermote, Y. J. Kaufman, D. Tanre and V. Kalbe. "Aerosol Retrieval Over Land from AVHRR Data – Application for Atmospheric Correction." *IEEE Transactions on Geoscience and Remote Sensing*, 30, 212–222, 1992.
- IPCC (Intergovernmental Panel on Climate Change), 1995: "Radiative Forcing of Climate Change," *Climate Change 1994*, Houghton, J. T., L. G. Meira Filho, J. Bruce, H. Lee, B. A. Callendar, E. Haites, N. Harris, and K. Maskell, Eds., Cambridge University Press, Cambridge, pp. 1-231, 1995.
- IPCC, 1996: *Climate Change 1995: The IPCC Second Assessment Report*, Cambridge University Press, in press, 1996. Advance copy of Summary for Policymakers: The Science of Climate Change, IPCC Working Group I (1995) available on <http://www.unep.ch/ipcc/sumwg1.html>.
- Jaenicke, R, Tropospheric aerosols, *Aerosol-cloud-climate interactions*, Ed., P. V. Hobbs, Academic Press, New York, 1-31, 1993.
- Johnston, P. V. R. L. McKenzie, J. G. Keys, and A. W. Matthews, Observations of depleted stratospheric NO<sub>2</sub> following the Pinatubo volcanic eruption, *Geophys. Res. Lett.*, 19, 211-213, 1994.
- Kaufman, Y. J. "Remote Sensing of Direct and Indirect Aerosol Forcing." *Aerosol Forcing of Climate*, eds. R. J. Charlson and J. Heintzenberg, pp. 297-332, John Wiley & Sons, Ltd., Chichester, U.K., 1995.
- Kent, G. S., C. R. Trepte, U. O. Farrukh, and M. P. McCormick, Variation in the stratospheric aerosol associated with the north cyclonic polar vortex as measured by the SAM II satellite sensor, *J. Atmos. Sciences*, 42, 1536, 1985.
- Kent, G. S., and S. K. Schaffner, Analysis of Atmospheric Dynamics and Radiative Properties for Understanding Weathered Climate, STX Tech. Rep. 2175, January 1988.



- Kent, G. S. and M. P. McCormick, Separation of cloud and aerosol in two-wavelength satellite occultation data, *Geophys. Res. Lett.* 18, 428-431, 1991.
- Kent, G. S., M. P. McCormick, and S. K. Schaffner, Global optical climatology of the free tropospheric aerosol from 1.0-mm satellite occultation measurements, *J. Geophys. Res.*, 96, 5249-5267, 1991.
- Kent, G. S., D. M. Winker, M. T. Osborn, and K. M. Skeens, A model for the separation of cloud and aerosol in SAGE II occultation data. *J. Geophys. Res.*, 98, 20725-20735, 1993.
- Kent, G. S., P. H. Wang, M. P. McCormick, and K. M. Skeens, Multiyear measurements of upper tropospheric aerosol characteristics, *J. Geophys. Res.*, 100, 13875-13899, 1995.
- King, M. D., Y. J. Kaufman, P. Menzel, and D. Tanre, Determination of cloud, aerosol, and water vapor properties from the Moderate Resolution Imaging Spectrometer (MODIS), *IEEE Trans. Geosci. Rem. Sens.*, 30, 2-27, 1992.
- Kinne, S., O. B. Toon, and M. J. Prather, Buffering of stratospheric circulation by changing amounts of tropical ozone - a Pinatubo case study, *Geophys. Res. Lett.*, 19, 1927-1930, 1992.
- Kinnison, D. E., K. E. Grant, P. S. Connell, D. A. Rotman, D. J. Wuebbles, The chemical and radiative effects of the Mount Pinatubo eruption, *J. Geophys. Res.*, 99, 25,705-25,731, 1994.
- Koike, M., Y. N. B. Jones, W. A. Matthews, P. V. Johnston, R. L. McKenzie, D. Kinnison, and J. Rodriguez, Impact of Pinatubo aerosol on the partitioning between  $\text{NO}_2$  and  $\text{HNO}_3$ , *Geophys. Res. Lett.*, 21, 597-600, 1994.
- Komhyr, W. D., R. D. Grass, R. D. Evans, R. K. Leonard, D. M. Quincy, Unprecedented 1993 ozone decrease over the United States from Dobson spectrophotometer observations, *Geophys. Res. Lett.*, 21, 201-204, 1994.
- Labitzke, K., B. Naujokat, and M. P. McCormick, Temperature effects on the stratosphere of the April 4, 1982 eruption of El Chichon, Mexico, *Geophys. Res. Lett.*, 10, 24, 1983.
- Labitzke, K. and M. P. McCormick, Stratospheric temperature increases due to Pinatubo aerosols, *Geophys. Res. Lett.*, 19, 207-210, 1992.
- Lin, N. H., and V. K. Saxena, Characteristics of Antarctic stratospheric aerosols during the 1987 ozone depletion episode based on SAGE II satellite observations, *J. Geophys. Res.*, 97, 7635-7649, 1992.
- Livingston, J. M., and P. B. Russell, Retrieval of aerosol size distribution moments from multiwavelength particulate extinction measurements, *J. Geophys. Res.*, 94, 8425-8433, 1989.

- Martonchik, J. V., and D. J. Diner, Retrieval of aerosol and land surface optical properties from multiangle satellite imagery, *IEEE Trans. Geosci. Rem. Sens.*, 30, 223-230, 1992.
- Mauldin, L. E., Stratospheric Aerosol and Gas Experiment II instrument: a functional description, *Opt. Eng.*, 24, 2, 307-312, 1985.
- Mauldin, L. E., M. P. McCormick, J. M. Zawodny, L. R. McMaster, W. P. Chu, J. C. Gustafson, and G. L. Maddrea, The Stratospheric Aerosol and Gas Experiment III instrument proposed for EOS: a conceptual design, Int. Congress on Opt. Sci. and Eng. - Paris, France, 1989.
- McCormick, M. P., P. Hamill, T. J. Pepin, W. P. Chu, T. J. Swissler, and L. R. McMaster, Satellite studies of the stratospheric aerosol, *Bull. of the Amer. Met. Soc.*, 60, 9, 1979.
- McCormick, M. P., W. P. Chu, G. W. Grams, P. Hamill, B. M. Herman, L. R. McMaster, T. J. Pepin, P. B. Russell, H. M. Steele, and T. J. Swissler, High-latitude stratospheric aerosol measured by SAM II satellite system in 1978-1979, *Science*, 214, 328-331, October, 1981.
- McCormick, M. P., H. M. Steele, P. Hamill, W. P. Chu, T. J. Swissler, Polar stratospheric cloud sightings by SAM II, *J. Atmos. Sci.*, 39, 6, 1387, 1982.
- McCormick, M. P., SAGE II: an overview, *Adv. Space Res.*, 7, 3, (3)219-(3)226, 1987.
- McCormick, M. P., et al Stratospheric Aerosol and Gas Experiment III (SAGE III) aerosol and trace gas measurements for Earth Observing System (EOS),, SPIE Paper No. 1491-16, 1991.
- McCormick, M. P., J. M. Zawodny, W. P. Chu, J. W. Baer, J. Guy, and A. Ray, Stratospheric Aerosol and Gas Experiment III (SAGE III), SPIE International Symposium for Optical Engineering - Orlando, FL, 1993.
- McCormick, M. P., P.-H. Wang, and L. R. Poole, Stratospheric Aerosols and Clouds, in Aerosol-Cloud-Climate Interactions, P. V. Hobbs, Editor, Academic Press, San Diego, CA, 205-222, 1993.
- McCormick, M. P., L. W. Thomason, and C. R. Trepte, Atmospheric effects of the Mt. Pinatubo eruption, *Nature*, 373, 399-404, 1995.
- McElroy, M. B., R. J. Salawitch, and C. Wofsy, Antarctic O<sub>3</sub>: Chemical Mechanisms for the spring decrease, *Geophys. Res. Lett.*, 13, 1296, 1986.
- Minnis, P., D. F. Young, E. F. Harrison, Examination of the relationship between outgoing infrared window and total longwave fluxes using satellite data, *J. Climate*, 4, 1114-1133, 1991.
- MISR Level 2 Algorithm Theoretical Basis: Aerosol/Surface Product, Part 1 (Aerosol Product) JPL D-11401, Jet Propulsion Laboratory, California Institute of Technology, Pasadena, CA, 1995.

- Mohnen, V. A., Stratospheric ion and aerosol chemistry and possible links with cirrus cloud microphysics - a critical assessment, *J. Atmos. Sci.*, 47, 1933-1948, 1990.
- NRC (National Research Council), 1994: *Atmospheric Effects of Stratospheric Aircraft*, National Academy Press, Washington, DC, 45 pp., 1994.
- NRC (National Research Council), 1996: *A Plan for a Research Program on Aerosol Radiative Forcing and Climate*, National Academy Press, Washington, DC, 161 pp., 1996.
- Pepin, T. J. and M. P. McCormick, Stratospheric Aerosol Measurement Experiment MA-007, NASA TM X-58173, February, 1976
- Pinnick, R. G., J. M. Rosen, and D. J. Hofmann, Stratospheric aerosol measurements, III: Optical model calculations, *J. Atmos. Sci.*, 33, 304-314, 1976.
- Plumb, R. A., A tropical pipe model of stratospheric transport, *J. Geophys. Res.*, 101, 3957-3972, 1996.
- Pollack, J. B., and T. P. Ackerman, Possible effects of the El Chichon volcanic cloud on the radiation budget of the northern tropics, *Geophys. Res. Lett.*, 10, 1057, 1983.
- Poole, L. R., and M. P. McCormick, Polar stratospheric clouds and the Antarctic ozone hole. *J. Geophys. Res.*, 93, 8423, 1988.
- Poole, L. R., and M. Pitts, Polar stratospheric cloud climatology based on Stratospheric Aerosol Measurement II observations from 1978 to 1989, *J. Geophys. Res.*, 99, 13083-13089, 1994.
- Pueschel, R. F., K. G. Snetsinger, J. K. Goodman, O. B. Toon, G. V. Ferry, V. R. Oberbeck, J. M. Livingston, S. Verma, W. Fong, W. L. Starr, and K. R. Chan, Condensed nitrate, sulfate, and chloride in Antarctic stratospheric aerosols, *J. Geophys. Res.*, 94, 11,271-11,284, 1989.
- Pueschel, R. F., K. G. Snetsinger, P. B. Russell, S. A. Kinne, and J. M. Livingston, The effects of the 1991 Pinatubo volcanic eruption on the optical and physical properties of stratospheric aerosols. *Proc. IRS92: Current Problems in Atmospheric Radiation*, S. Keevalik, editor, A. Deepak Publishing Co. 1992.
- Pueschel, R. F., J. M. Livingston, P. B. Russell, and S. Verma, Physical and optical properties of the Pinatubo volcanic aerosol: aircraft observations with impactors and a suntracking photometer. *J. Geophys. Res.*, 95, 12,915-12,922, 1994.
- Oberbeck, V. R., J. M. Livingston, P. B. Russell, R. F. Pueschel, J. N. Rosen, M. T. Osborn, T. J. Swissler, M. A. Kritz, K. G. Snetsinger, and G. V. Ferry, SAGE II aerosol validation: Selected altitude measurements, including particle micro-measurements, *J. Geophys. Res.*, 94, 8367-8380, 1989.
- Osborn, M. T., DeCoursey, C. R. Trepte, D. M. Winker, and D. C. Woods, Evolution of the Pinatubo volcanic cloud over Hampton, Virginia, *Geophys. Res. Lett.*, 22, 1101-1104, 1995.

- Rao, C. R. N., L. L. Stowe and E. P. McClain. "Remote Sensing of Aerosols Over the Oceans Using AVHRR Data: Theory, Practice and Applications." *Int. J. Remote Sens.*, 10, 4-5, 743-749, 1989.
- Rinsland, C. P., G. K. Yue, M. R. Gunson, R. Zander, and M. C. Abrams, Mid-Infrared Extinction by Sulfate Aerosols from the Mt. Pinatubo Eruption, *J. Quant. Spectrosc. Radiat. Transfer*, 52, 241-252, 1994.
- Robock, A., Energy balance climate model calculations of the effects of the El Chichon eruption, *Geof. Int.*, 23, 403, 1984.
- Russell, P. B., T. J. Swissler, M. P. McCormick, W. P. Chu, J. M. Livingston, and T. J. Pepin, Satellite and correlative measurements of the stratospheric aerosol, I. An optical model for data conversion, *J. Atmos. Sci.*, 38, 1279-1294, 1981.
- Russell, P. B., J. M. Livingston, R. F. Pueschel, J. B. Pollack, S. L. Brooks, P. J. Hamill, J. J. Bauman, L. W. Thomason, L. L. Stowe, T. Deshler, E. G. Dutton, and R. W. Bergstrom, Global to microscale evolution of the Pinatubo volcanic aerosol, derived from diverse measurements and analyses, *J. Geophys. Res.*, 101.
- SAGE II Monthly Profile User's Guide, Version 5.6, January 3, 1990, NASA Langley Research Center, Hampton, VA 23668.
- Saxena, V. K., J. Anderson, and N.-H. Lin, Changes in Antarctic stratospheric aerosol characteristics due to volcanic eruptions as monitored by SAGE II satellite, *J. Geophys. Res.*, 100, 16,735-16,751, 1995.
- Shettle, E. P., and R. W. Fenn, Models for the aerosols of the lower atmosphere and the effects of humidity variations on their optical properties. AFGL-TR-79-0214, Air Force Geophysics Laboratory, 94 pp., 1979.
- Solomon, S., R. W. Portmann, R. R. Garcia, L. W. Thomason, L. R. Poole, and M. P. McCormick, The role of aerosol variations in anthropogenic ozone depletions at northern midlatitudes, *J. Geophys. Res.*, 101, 6713-6727, 1996.
- Steele, H. M., and P. Hamill, Effects of temperature and humidity on the growth and optical properties of sulfuric acid-water droplets in the stratosphere, *J. Aerosol Sci.*, 12, 517-528, 1981.
- Stolarski, R. S., and H. L. Wesoky, The atmospheric effects of stratospheric aircraft: A third program report, NASA Reference Publication 1313, 1993.
- Strong, A. E., Monitoring El Chichon Aerosol Distribution Using NOAA-7 Satellite AVHRR Sea Surface Temperature Observations, *Geof. Int.*, 23, 129, 1984.
- Svenningsen, I. B., H.-C. Hansson, and A. Wiedensohler, Hygroscopic growth of aerosol particles in the Po Valley, *Tellus*, 44B, 556-569, 1992.
- Thomason, L. W., and L. R. Poole, On the use of stratospheric aerosol properties as diagnostics of Antarctic vortex processes, *J. Geophys. Res.*, 98, 23003-23012, 1993.

- Thomason, L. W., G. S. Kent, C. R. Trepte, and L. R. Poole, A comparison of the stratospheric aerosol background periods of 1979 and 1989-1991, in press, 1996.
- Toon, O. B., P. Hamill, R. P. Turco, and J. Pinto, Condensation of  $\text{HNO}_3$  and  $\text{HCl}$  in the winter polar stratosphere, *Geophys. Res. Lett.*, 13,1284, 1986.
- Trepte, C. R., and M. H. Hitchman, Tropical stratospheric circulation deduced from satellite aerosol data, *Nature*, 355, 626-628, 1992.
- Trepte, C. R., R. E. Veiga, and M.P. McCormick, The poleward dispersal of Mount Pinatubo volcanic aerosol. *J. Geophys. Res.*, 98, 18,563-18,573, 1993.
- Turco, R. P., R. C. Whitten, and O. B. Toon, Stratospheric aerosols: Observation and theory, *Rev. Geophys. and Space Phys.*, 20, 233-279, 1982.
- Trepte, C. R., L. W. Thomason, and G. S. Kent, Banded structures in stratospheric aerosol distributions, *Geophys. Res. Lett.*, 21, 2397-2400, 1994.
- Twomey, S., On the numerical solution of Fredholm integral equation of the first kind by the inversion of the linear system produced by quadrature, *J. Assoc. Comput. Mach.*, 10, 97-101, 1963.
- Twomey, S., Comparison of constrained linear inversion and an iterative nonlinear algorithm applied to the indirect estimation of particle size distributions, *J. Comput. Phys.*, 18, 188-198, 1975.
- Twomey, S., Introduction to the mathematics of inversion in remote sensing and indirect measurements, 243 pp., Elsevier Science, New York, 1992
- Wang, M., and H. R. Gordon, 1994. Estimating aerosol optical properties over the oceans with MISR: Some preliminary studies, *Appl. Opt.*, 33, 4042-4057, 1994.
- Wang, P.-H., M. P. McCormick, T. J. Swissler, M. T. Osborn, W. H. Fuller, and G. K. Yue, Inference of stratospheric aerosol composition and size distribution from SAGE II satellite measurements, *J. Geophys. Res.*, 94, 8435-8446, 1989.
- Wang, P.-H., SAGE II tropospheric measurement frequency and its meteorological implication, *Preprints, 7th Conf. Sat. Met. Oceanog.*, J15-J18, Am. Meteor. Soc., Boston, 1994.
- Wilson, J. C., et al., In situ observations of aerosol and  $\text{ClO}$  after the 1991 eruption of Mount Pinatubo: effect of reactions on sulfate aerosol, *Science*, 261, 1140-1143, 1993.
- World Meteorological Organization, Report of the experts meeting on aerosols and their climatic effects, Eds. A. Deepak and H. Gerber, WCP-55, 1983.
- World Meteorological Organization, WMO Rep. 16, 1985.
- Young, A. T., Revised depolarization corrections for atmospheric extinction, *Appl. Opt.*, 19, 3427-3430, 1980.

- Yue, G. K., and A. Deepak, Retrieval of stratospheric aerosol size distribution from atmospheric extinction of solar radiation at two wavelengths, *Appl. Opt.* 22, 1639-1645, 1983.
- Yue, G. K., and A. Deepak, Latitudinal and altitudinal variation of size distribution of stratospheric aerosols inferred from SAGE aerosol extinction coefficient measurements at two wavelengths, *Geophys. Res. Lett.*, 11, 999-1002, 1984.
- Yue, G. K., M. P. McCormick, and W. P. Chu, Retrieval of composition and size distribution of stratospheric aerosols with the SAGE II satellite experiment, *J. Atmos. Oceanic Techn.*, 3, 371-380, 1986.
- Yue, G. K., L. R. Poole, P.-H. Wang, and E. W. Chiou, Stratospheric aerosol acidity, density, and refractive index deduced from SAGE II and NMC temperature data, *J. Geophys. Res.*, 99, 3727-3787, 1994.

## Appendix A. SAGE III Instrument Description

The design of the SAGE III sensor relies heavily upon the flight proven designs used in the SAM II and SAGE I/II instruments. Specifically, the separate sensor and electronics modules concept from SAGE II is utilized, as are the grommet isolation and contamination door designs. Additionally, the SAGE II pointing system and scan mirror designs are reused, with certain necessary modifications (primarily an attenuator filter) to permit solar and lunar observations with the same detector assembly.

The SAGE III sensor assembly, illustrated in Figure A-1, consists of a sun-tracker, telescope, and grating spectrometer with a CCD detector array; the mass is estimated at 35 kg., a volume of 6000 cm<sup>3</sup>, with an average power of 60 W and a peak power of 75 W. The two-axis passive sun-tracker, with a scan mirror that scans the instrumental field of view across the solar disk, obtains multiple samples at each altitude, improving the measurement precision. Sunspots are readily detected by scanning, rather than staring at the Sun. A pictorial representation of the scanning pattern as a function of tangent altitude and the corresponding detector output (single wavelength) is illustrated in Figure A-2. The two solid lines denote the position of the top and bottom of the solar disk during a sunrise event as viewed from the spacecraft. The gradual expansion of the vertical sun shape is due to atmospheric refraction. The ordinate denotes the tangent altitude, while the abscissa denotes the event time. During an occultation event, the instrument scans the solar disk as indicated by the dashed line in the figure.

The telescope and spectrometer are illustrated in Figure A-3 and constitute new designs optimized to meet the requirements of lunar occultation measurements. The telescope is a f/4 Dall-Kirkham configured design chosen for its ease of alignment; the speed represents a tradeoff between optimum performance and spectral imaging. The spectrometer is a new design, utilizing a holographic, aberration reduced, grating to provide stigmatic imaging at 440 and 868 nm with 1 nm resolution below 450 nm and 2 nm resolution between 740 and 960 nm. The grating is formed on a spherical substrate with a radius of 152 mm and is imaged through a field flattener and order-sorting filters onto the CCD detector. The grating is utilized in the first positive order with diffraction angles between 8.3 and 17.0 degrees; a ruling of 199 lines per millimeter yields a dispersion of 0.94 to 1.88 nm per pixel in the focal plane (depending on wavelength). Evaluation gratings have been tested and demonstrate near-theoretical first-order efficiencies with very low scattered light properties. The spectrometer has been ray-traced and a Monte Carlo simulation of optical tolerances has been performed which indicates that at the wavelengths of best spectral focus, a FWHM bandpass of less than 1.2 nm per pixel should be achievable.

The detector assembly consists of two elements, a Tektronix 800x10 pixel backside-illuminated, thinned CCD array for the 280 - 1040 nm spectral region and a InGaAs

infrared photodiode (1550  $\pm$  15 nm) that are spatially co-registered. The 800 elements of the array provide the spectral information, the 10 pixels aligned along the horizontal direction are summed together and can be considered a single long pixel. Practical considerations favor pixel subdivision: large pixels can have a low charge transfer efficiency which can be avoided through subdivision, and secondly reducing the horizontal instantaneous field of view (IFOV) can improve the probability of cloud-free measurements. Consequently, in the solar occultation mode, 3 pixels (0.5x1.5 arcminute IFOV) are used to improve the frequency of penetration of the measurements into the troposphere. In contrast, for the lunar occultation measurements, all 10 pixels are used to collect more light.

In the solar occultation mode, the optical throughput of the instrument (grating efficiency and CCD quantum efficiency) combined with the spectral variation in the solar spectrum produce a wide variation in the rate of charge accumulation in the CCD pixels as a function of wavelength. Optimum performance (signal-to-noise ratio and dynamic range) of the detector is achieved when pixels are operated at or near full well. To obtain full well across the spectral region, a spectral flattening filter was considered to selectively attenuate the spectrum near the middle of the spectral band pass, but was determined to be too difficult to design. Instead, the array has been divided into eight segments that have individually controlled integration times to control the filling of the wells. Each segment is operated at or near full well, and the transitions between segments are chosen to avoid potential science channels. This solution optimizes performance and eliminates an item of significant risk and cost.

The lunar occultation measurements are significantly more complicated than the solar measurements; depending upon phase, the Moon is between one million and ten million times less luminous than the Sun, and the lunar albedo is non-uniform making determination of atmospheric transmission non-trivial. The instrument is designed to compensate for this large change in illumination in part by removing the solar attenuator (a neutral density filter with an attenuation of 100) from the optical path. In addition, the integration time is increased from 0.09-2.2 milliseconds to 62 milliseconds (with a resulting increase in signal of 28 to 500), and the instrumental field of view is increased from 3 pixels to 10 pixels (producing an increase of 3.3 in signal level). The resulting gain increase of 165,000 should permit lunar measurements with a signal-to-noise ratio of 150-300, only a factor of 10-20 times poorer than the solar measurements which implies that the altitude range for the species retrievals will be somewhat reduced in the lunar occultation mode.

The detector package has been modeled and electrical, optical, thermal, and radiation-shielding testing of prototype detectors has been performed. The detector assembly is surrounded by an aluminum radiation shield (nominally 1-inch thick) and is illustrated in Figure A-4. The housing is comprised of a base plate, a lead frame assembly, and an optical field flattener. The lead frame assembly is an insulating rectangle through which



the electrical connections to the detector and a thermoelectric cooler (TEC) pass. The field flattener is a plano-concave sapphire window. The purpose of the field flattener, in addition to providing a window to the sealed CCD package, is to further increase the radius of curvature of the focal field and coincide better with the planar CCD array.

Mounted to the backside of the field flattener are three order-sorting filters that provide the out-of-band rejection of light diffracted towards the focal plane assembly from other grating orders. The CCD is mounted to a TEC that is, in turn, mounted to the base plate heat sink. The CCD is designed with built-in thermistors that are part of an active temperature control system to meet the stability and end-of-life dark current requirements. The detector assembly has been included in the stray light analysis of the spectrometer, which showed that a significant reduction in the amount of scattered light could be achieved by rotating the CCD about its long axis by 11 degrees and eliminating internal reflections within the detector assembly. Also within the detector assembly is the InGaAs photodiode for the 1540 nm channel. This channel lies in the zeroth-order beam and has its band pass determined by a filter in much the same manner as was done with two of the channels in SAGE II. This detector is within the assembly because of the close proximity of the zeroth-order light rays to the end of the CCD array. Prototype detectors have been manufactured and tested for spectral quantum efficiency, dark current versus temperature, full-well capacity, charge transfer efficiency, and linearity. Radiation testing with monoenergetic proton beams of differing total doses have assessed the performance in a radiation environment, and led to models of energetic particle transport and secondary particle production, and an assessment of the shielding requirements for the CCD. In addition, models were developed to describe the observed temperature dependent gain of the field effect transistor preamplifiers on the CCD.

The spectrometer with the CCD array of detectors provides continuous wavelength coverage between 280 and 1040 nm and will permit the measurement of multiple absorption features of each gaseous species and multi-wavelength measurements of broadband extinction by aerosols. In the present configuration, 12 solar channels ( 80 sub-channels) will be routinely utilized in the solar occultation measurements and 3 channels (340 sub-channels) in the lunar occultation measurements, greatly decreasing the random error in the measurements (precision), and allowing for more accurate modeling of the multi-wavelength aerosol extinction. Included within the instrument band pass is the O<sub>2</sub> A band (around 760 nm) which will permit the retrieval of density and temperature with which the viewing geometry (as a pressure level) can be inferred. This improvement over SAGE II, which relied upon the NOAA gridded analyses, should improve the accuracy of the SAGE III profiles and simplify the comparison with other measurements. Additionally, the linear array of detectors will permit on-orbit wavelength and intensity calibration from observations of the exo-atmospheric solar Fraunhofer spectrum. The continuous spectral calibration, combined with the self-calibrating nature of the occultation technique (ratioing the signal transmitted through the atmosphere to the exo-atmospheric reference signal for each measurement) makes SAGE III ideal for long-term

monitoring of trends in ozone and other gas species, which is a central objective of the EOS program.

The expanded spectral coverage of the SAGE III instrument permits the observation of  $O_3$  in the mesosphere between 65 and 85 km by utilizing the UV absorption in the short wavelength region between 385 and 290 nm and, combined with a fixed channel InGaAs detector at 1550 nm, should greatly enhance the characterization of multi-wavelength aerosol and clouds and extend this capability to lower altitudes in the troposphere. The CCD array will provide approximately 2-nm resolution in the spectral region between 920 and 960 nm. In combination with an increase in digitization from 12 bit precision to 16 bit precision, this should allow for greater discrimination of water vapor from aerosol (both volcanic and thin cloud), and better retrieval of the higher water vapor values at lower altitudes in the troposphere than was possible with SAGE II. Table A.1 details the measurement capability of SAGE III for single profile retrievals. The notable difference, as discussed above, is the determination of pressure and temperature from oxygen A band and the improved precision from the inclusion of additional channels.

With a 16-bit A/D converter, the SAGE III spectrometer will allow for variable integration time and on-orbit gain programming necessary for lunar observations. This potentially doubles the number of measurements per orbit, but requires a detector and signal chain that can accommodate the reduced flux observed during lunar occultations. In lunar occultation SAGE III will monitor  $O_3$ ,  $NO_2$ , pressure, and  $H_2O$ , as well as  $OCIO$  and  $NO_3$ .

**Table A.1: SAGE III Measurement Capability (single profile)**

Channel	Wavelength (nm)	Products	Solar Altitude	Error (%)	Lunar Altitude (km)	Error (%)
S1	290	O <sub>3</sub>	50-85	10	----	----
S2	385	Aerosol	15-40	10	----	----
L1	380-420	OCIO	----	----	15-25	25
S3/L1	433-450	NO <sub>2</sub> , Aerosol	10-50, 10-40	10 ----	20-50	10
L1	470-490	O <sub>3</sub>	----	----	16-35	10
S4	521	Aerosol, Cloud	6-40	10 ----	----	----
S5	560-616	O <sub>3</sub>	6-60	5	----	----
L1	640-680	NO <sub>3</sub>	----	----	20-55	10
S6	670	Aerosol	3-40	5	----	----
S7	758	Aerosol	3-40	5	----	----
S8/L2	759-771	Pressure, Temperature	0-85, 0-85	2K 2K	6-40 6-40	2 6
S9	869	Aerosol	0-40	5	----	----
S10/L3	933-960	H <sub>2</sub> O,	0-50,	10	6-25	15
S11	1020	Aerosol, Cloud	0-40	5	----	----
S12	1540	Aerosol, Cloud	0-40	5	----	----

a. Error is estimated precision

b. Lowest altitude is determined by cloud top height

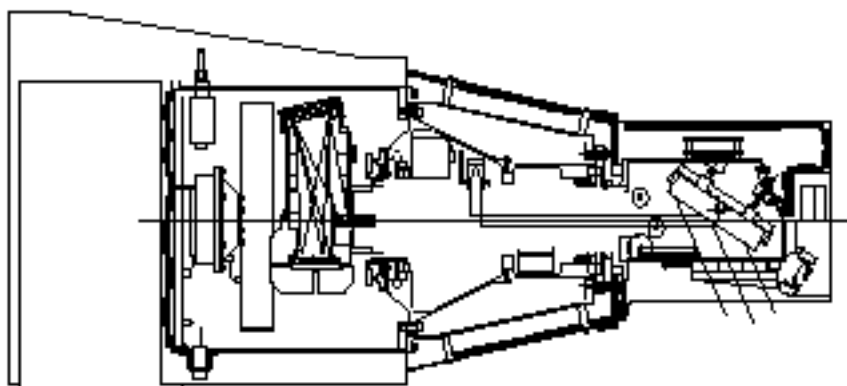


**Figure A-1.** The SAGE III sensor assembly.

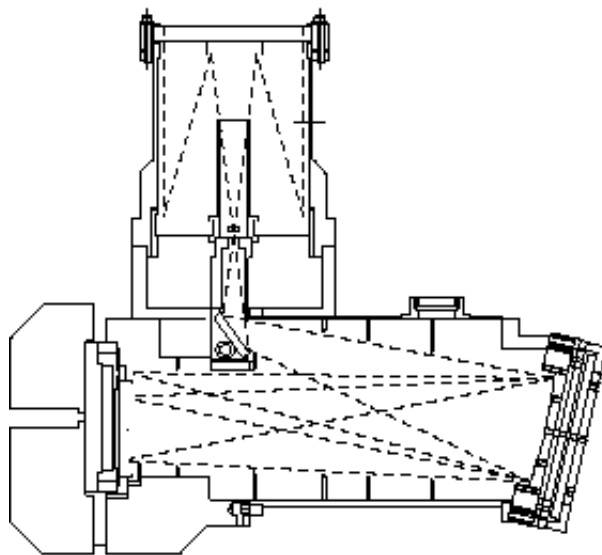


**Figure A-2.** Optical configuration and ray paths for the SAGE III telescope and spectrometer.

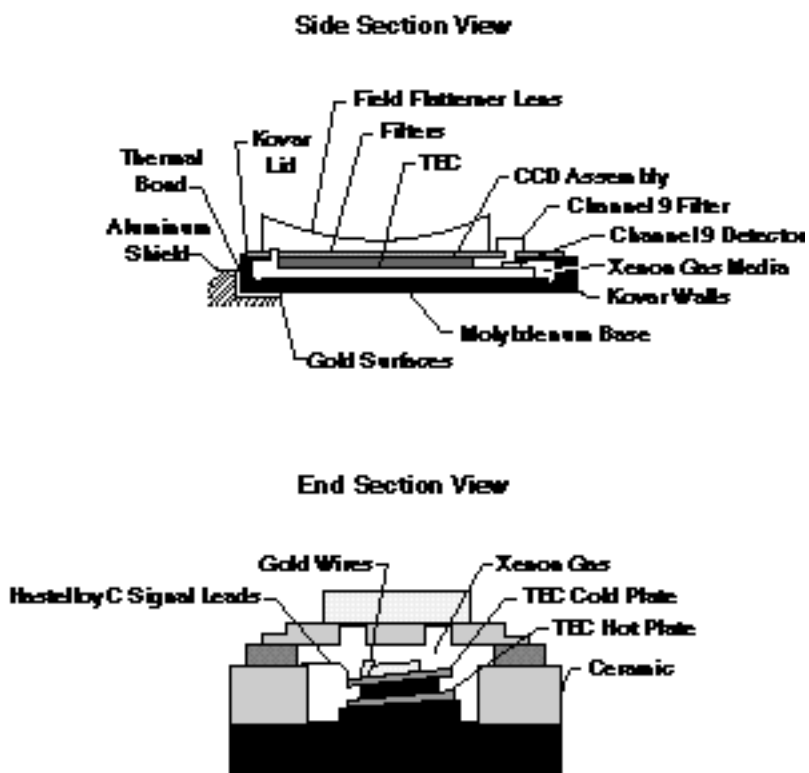


**Figure A3.** SAGE III detector package.

## Appendix B. Implimentation of Atmospheric Retrievals

The retrieval of channels which involve spectroscopic simulation of individual spectral lines employs the technique of Gordley and Russell (1980). This technique involves the precalculation of a grid of transmissions as a function of temperature, pressure and mass path. From the observed atmospheric absorption and an assumed temperature and pressure of a layer, the mass path through a homogenous layer is obtained from precalculated tables. This involves a reverse interpolation in temperature, pressure and mass path within these precalculated tables.

A linear interpolation is not, in general, sufficient. Instead, a second order reverse interpolation is performed by a Taylor series expansion around the closest point in the matrix.

$$\begin{aligned}
 V_{obs} = V_{ijk} &+ \frac{V_{ijk}}{T} (T - T_i) + \frac{V_{ijk}}{p} (p - p_j) + \frac{V_{ijk}}{u} (u - u_k) \\
 &+ \frac{{}^2V_{ijk}}{2T} (T - T_i)^2 + \frac{{}^2V_{ijk}}{2p} (p - p_j)^2 + \frac{{}^2V_{ijk}}{2u} (u - u_k)^2 \times \frac{1}{2} \\
 &+ \frac{{}^2V_{ijk}}{T p} (T - T_i)(p - p_j) + \frac{{}^2V_{ijk}}{T u} (T - T_i)(u - u_k) + \frac{{}^2V_{ijk}}{p u} (p - p_j)(u - u_k)
 \end{aligned} \tag{1}$$

Here  $V_{obs}$  is the observed transmission, the transmission at the nearest grid point,  $i, j$  and  $k$  the indices of the nearest grid point in temperature, pressure and mass path, respectively,  $T_i, p_j$  and  $u_k$  the temperature, pressure and mass path, respectively, used in the computation of the nearest grid point, and  $T, p$  and  $u$  the temperature, pressure and mass path corresponding to the observed transmission. All quantities are known except  $u$  and this equation forms a quadratic equation in  $u$ . Rather than determine the derivatives in this equation by finite differences involving individual transmission values in the precomputed matrix, nine parallel matrices of all of the first and second derivatives in this equation are also precalculated over the same grid. The grid spacings in temperature, pressure and mixing ratio are sufficiently fine that the interpolation from the precalculated derivatives are accurate to within the SAGE III observed uncertainty.

The nine derivatives above are found in a manner analogous to the case of fitting laboratory spectra described by Benner et al. (1995). For  $N$  spectral lines the transmission at a specific wavenumber,  $V$ , is the product of the transmission of each spectral line,  $V_i$ , at that wavenumber.

$$V = \sum_{i=1}^N V_i \quad (2)$$

Differentiating both sides yields an expression for the derivative of the transmission with respect to a parameter,  $x$ , which is used in the calculation of the transmission.

$$\frac{V}{x} = \sum_{i=1}^N \frac{V}{V_i} \frac{V_i}{x} \quad (3)$$

This only requires that the derivative with respect to transmission be found for each spectral line individually. An equation may be derived for the second derivatives in a similar manner. The derivative for an individual spectral line is straightforward, although complicated at times. For example, SAGE III uses only Voigt spectral line shapes. The  $n$ th derivative for a Voigt spectral line with respect to the mass path,  $u$ , can be expressed in terms of only the transmission itself, the mass path and  $n$ .

$$\frac{{}^n V_i}{u^n} = \frac{1nV_i}{u} {}^n V_i \quad (4)$$

This expression provides two of the nine required derivatives. The remaining seven derivatives involve at most only algebraic variations of the physical conditions, the spectral line parameters, the transmission and the real and imaginary parts of the complex error function. The real part of the complex error function is just the Voigt function which was used in the calculation of the transmission. Calculating both the real and imaginary parts of the complex error function requires less than twice the time required to calculate the real part.

The light falling upon a single pixel of the CCD cannot be treated as monochromatic. The transmission and derivatives must apply over a finite range of wavelength with the appropriate point spread function,  $(\lambda)$ , applied. This is approximated by calculations of the transmission and its derivatives at  $n$  specific wavelengths and it is assumed that these values are constant over a finite spectral interval,

$\lambda_i$ .

$$Y_{mean} = \frac{\sum_{i=1}^n (\lambda_i) Y_i (\lambda_i)}{\sum_{i=1}^n (\lambda_i)} \quad (b.5)$$

Here  $Y$  may represent either the transmittance or one of its derivatives.

The pressure, temperature and/or mass path as a function of position in the atmosphere are retrieved by means of a global least squares solution. The least squares process requires

the derivative of the calculated transmission with respect to each unconstrained parameter at each observed atmospheric point. These derivatives are supplied directly by interpolation in the precomputed derivative matrix. First order interpolation is done using a Taylor series expansion and the tabulated second derivatives. For example, the derivative of the transmission with respect to temperature requires four table lookups for derivatives.

$$\frac{V}{T} = \frac{V_{ijk}}{T} + \frac{{}^2V_{ijk}}{T} (T - T_i) + \frac{{}^2V_{ijk}}{T p} (p - p_j) + \frac{{}^2V_{ijk}}{T u} (u - u_k) \quad (6)$$

The derivative of the transmission with respect to a physical parameter in a given layer is insufficient in itself for the global least squares retrieval. The derivative of the transmission of a ray in the occultation mode with respect to a physical parameter in a specific layer requires that the derivative be propagated in the manner of Gordley and Russell (1980) through the atmosphere. For example, the derivative of the transmission  $V$  after the final layer  $N$  with respect to parameter  $x$  from layer  $i$  ( $1 \leq i \leq N$ ) is accomplished with a series of derivatives of the transmission with respect to mass path in the precalculated table.

$$\frac{V_N}{x_i} = \frac{V_i}{x_i} + \sum_{j=i}^{N-1} \frac{(V/u)_{T_{j+1}, p_{j+1}, V_{j+1}}}{(V/u)_{T_{j+1}, p_{j+1}, V_j}} \quad (7)$$

For  $i = N$ , the derivative is zero.

## References

- Benner, D. C., C. P. Rinsland, V. Malathy Devi, M. A. H. Smith and D. Atkins, A multispectrum nonlinear least squares fitting technique, *J. Quant. Spectrosc. Radiat. Transfer*, 53, 705-721, 1995.
- Gordley, L. L., and J. M. Russell, A fast and accurate radiance algorithm for applications to inversion of limb measurements, in *Remote Sensing of Atmospheres and Oceans*, edited by A. Deepak, p. 591, Academic Press, San Diego, Calif., 1980.

## Appendix C. Atmospheric Inhomogeneity

The SAGE III inversion algorithm, as do essentially all processing algorithms for limb viewing instruments, assumes that the atmosphere is spherically homogeneous. This is probably a good assumption for most stratospheric constituents but is not always true for cloud and may well be a poor approximation for other constituents in the troposphere. Of all the species measured by SAGE III, cloud is most likely to be affected by its own inhomogeneous nature. Despite this, the current SAGE III algorithm, essentially an

extension of that used for SAGE II (Kent et al., 1993), neglects this feature of cloud observations. Simulation studies are in progress that may lead to modifications in the cloud detection algorithm that exploit inhomogeneity as a tool to infer the presence of cloud. Inhomogeneous cloud, whether stratospheric or tropospheric, is likely to degrade the quality of concurrent SAGE III measurements of molecular species and temperature and pressure.

Airborne lidar data, taken on an approximately 8000 km flight path over the tropical Pacific, has been used to simulate high altitude SAGE II cloud measurements and their inversion. These simulations produce cloud extinction values similar in magnitude and distribution to those obtained from SAGE II. They also show the existence of three possible error conditions that result from the inhomogeneous nature of the cloud:

1. The true altitude of a cloud may be higher than that found as a result of the SAGE II inversion. Errors of 1 km or more occurred in ~40% of the data set.
2. The inverted cloud extinction may differ (biased low) from the volume averaged extinction along the horizontal ray path.
3. The presence of non-uniform or isolated cloud patches can result in an apparent negative inverted extinction value just below the cloud. Such values were observed in about one third of the simulations. The present SAGE II inversion scheme (bottom up Twomey-Chahine) suppresses these negative values but compensates by reducing the extinction value just above the offending level.

This work is presently being prepared for publication (Simulation of SAGE II cloud measurements using airborne lidar data, G. S. Kent, D. M. Winker, M. A. Vaughan, P.-H. Wang, and K. M. Skeens, 1996).

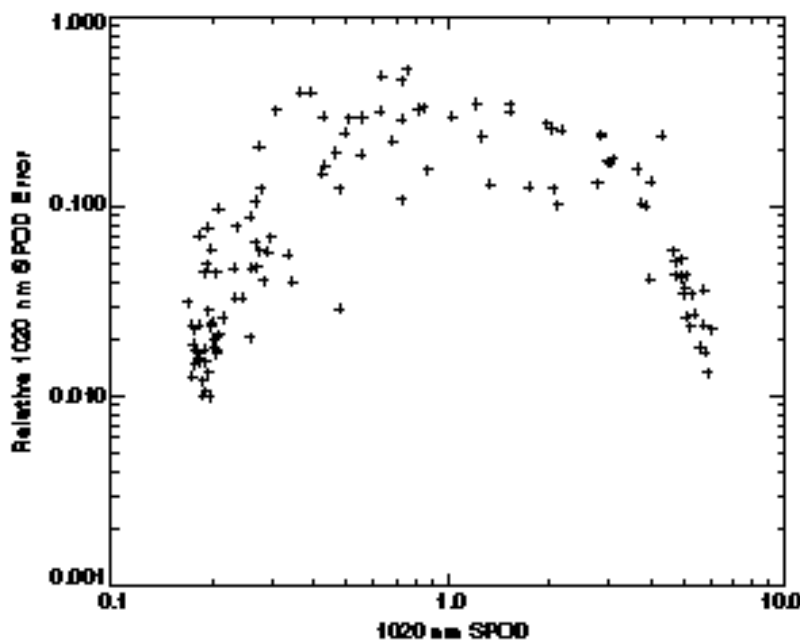
SAGE transmission measurements are an amalgamation of several independent scans across the Sun. In the presence of cloud or other inhomogeneities, these scans will measure different amounts of transmitted radiation from the same point on the Sun (because the spacecraft moves and the LOS at a given tangent altitude, as a result, also moves). These differences are manifested in the transmission data as an increased standard deviation relative to homogeneous conditions. The possibility exists that this variability may be used as an additional input to the cloud detection algorithm. The simulation described above has been extended to include spacecraft motion and compared to results from SAGE II observations.

Figure E.1 shows a scatter plot of SAGE II data at an altitude of 14.5 km in which the relative error in the slant path optical depth (SPOD) has been plotted against the SPOD itself. Low values of SPOD, corresponding to cloud-free observations, show low relative error. As cloud is observed in some scans, the relative error increases to a maximum as SPOD also increases. Then as more and more scans observe cloud, the relative error decreases as SPOD continues to increase. Figure E.2 shows the equivalent simulation using airborne lidar data. The behavior is very similar to that shown in Figure E.1.



Individual data points in this figure are color coded by their wavelength extinction ratio (525 to 1020 nm aerosol extinction ratio). This ratio is used as the primary discriminator between cloud and aerosol in SAGE II observations and is similar to that proposed for the SAGE III algorithm. We note that the majority of the high error cases (mixed cloud) would be identified as cloud due to their low extinction ratio. However, some high error cases have higher extinction ratios and would not be identified as cloud by the SAGE II algorithm though cloud is clearly present.

Based on these results, we plan to carry out further simulations of the effect of cloud and other inhomogeneities on the inversion algorithm and data quality (not only on cloud presence but also for all other detected species). In particular, we will investigate the effects of PSCs on data from the SAGE III/METEOR 3M flight. The outcome of further simulations may lead to modifications of the inversion algorithm (particularly for cloud detection) and error estimation. We will also consider the implication of cloud homogeneity on the SAGE III validation program (particularly its tropospheric section).



**Figure C-1** A scatter plot of SAGE II data at an altitude of 14.5 km, in which the relative error in the slant path optical depth (SPOD) is plotted against the SPOD itself. Data points cover both cloudy and non-cloudy situations.

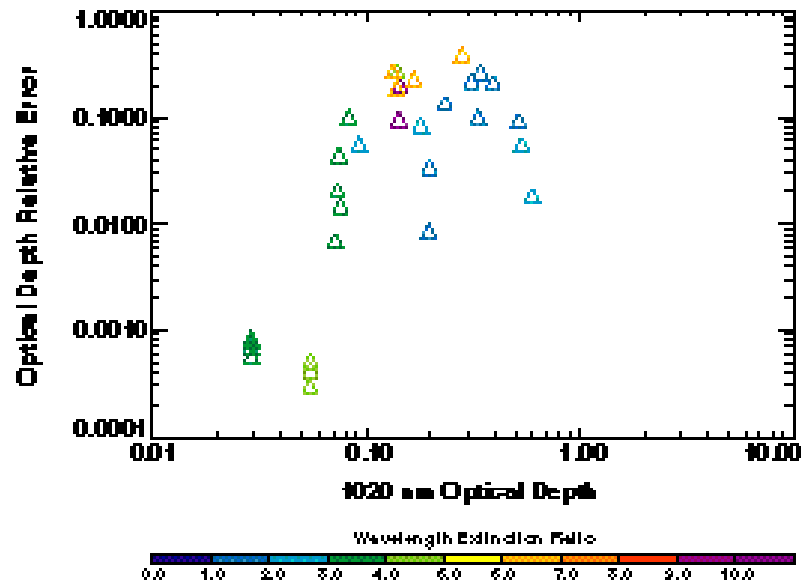


**Figure C-2** Scatter plot equivalent to that shown in figure E.1, but derived from simulations based on airborne lidar data obtained within a cloud field. The color coding shows the retrieved 525 to 1020-nm aerosol extinction ratio.

## **Appendix D. Molecular Absorption Cross-Sections: Spectroscopic Considerations for SAGE III**

### **D.1 Introduction**

This appendix reviews the current knowledge of molecular absorption cross sections as it pertains to the SAGE III [Stratospheric Aerosol & Gas Experiment] instrument, and is focused on the spectroscopic needs of the planned SAGE III measurements. This means the discussion is limited to those molecules and spectral regions that will be measured by the SAGE III instrument. Each of the individual molecules measured by SAGE III is discussed in a separate sections. However, each section addresses not only that part of the spectrum which is used to measure that gas but the rest of the spectrum where absorption by that species could interfere with the retrieval of other molecules.

### **D.2 Species Specific Information**

#### **D.2.1 Ozone**

##### **D.2.1.1 Ultraviolet**

The compilation of UV ozone cross-sections for LOWTRAN 7 and MODTRAN, by G.P. Anderson et al. (1989) is currently recommended, at least for wavelengths up to 345 nm. This compilation is primarily based on the data of Bass & Paur (1985) from 240 to 330, including a quadratic temperature dependence. Between 180 and 240 nm the measurements of Molina & Molina (1986) are used. The measurements of Molina & Molina (1986) and Yoshino et al. (1988) were used to extend the temperature dependent range to 340 nm, and preliminary data of Cacciani et al. (1987), [later published as Cacciani et al. (1989)], was to extend the wavelength coverage to 365 nm.

For wavelengths from 345 to 354 nm, the room temperature values in MODTRAN are consistent with those of Molina & Molina (1986) and with those of Cacciani et al. (1989). However there appears to be a problem with their temperature dependence for wavelengths greater than 345, resulting in a significant underestimate of the ozone absorption at stratospheric temperatures. The cause of this problem with the temperature dependence is not clear, [G.P. Anderson, private communication, 1996].

The recent room temperature measurements by Daumont et al. (1992) from 195 to 345 nm, agree within the stated accuracies with these earlier values. This group recently has extended these measurements to lower temperatures, [Malicet et al., 1998]. Burrows et al. (1999) have also measured the temperature dependence of ozone from 231 to 794 nm. These measurements, along with the recent accurate measurements of the ozone cross section for the 253.7 nm mercury line, by the University of Minnesota Group

[Mauersberger, et al. (1986 & 1987) and Barnes & Mauersberger, (1986)], should be used to re-examine the cross sections for this whole spectral region. The cross section at this mercury line based on Hearn's (1961) data was used to normalize the Bass & Paur (1985) data, along with a number of the earlier measurements.

Brion et al., [1998] have preliminary results continuing the room temperature measurements for ozone absorption from 345 nm to 830 nm. . These should be used to extend the ozone cross sections through the gap that currently exists in the available quantitative data between 360 and 410 nm.

The uncertainties in the UV data are generally within 1 to 2 % for wavelengths less than 325 nm. At longer wavelengths the uncertainties become increasingly larger as the values of the absorption cross section become smaller with increasing wavelength, and the uncertainties in the zero-absorption reference value become more significant. The uncertainties are nearly 10% by 345 nm, and greater than 20% for wavelengths greater than 350 nm. In the vicinity of the absorption minimum near the SAGE 385 nm aerosol channel, the uncertainties in the absorption cross section exceeds a factor of 2. However, at this wavelength the ozone absorption is negligible compared to the aerosol attenuation and is less than 5% of the typical aerosol extinction near 30 km (and the peak ozone mixing ratio).

#### **D.2.1.2 Visible and Near Infrared Cross-Sections:**

Recently there have been a several new spectroscopic studies of the ozone Chappuis and Wulf absorption bands, (S.M.Anderson et al., 1990, 1991,1993a, and Burkholder & Talukdar, 1994) along with measurements of the absolute cross-section at selected wavelengths near the peak of the Chappuis band, (Anderson & Mauersberger, 1992), and in the near IR, (S.M.Anderson et al., 1993b). Shettle & Anderson (1994) have used these to develop a new set of room temperature ozone absorption cross-sections. They normalized the spectral measurements to agree with the absolute cross-section data, within the measurement uncertainties, and smoothly joined the different sets of measurements, to provide the new cross-section over the spectral range from 407 to 1089 nm.

The accuracy of this data set is about 1 to 2% from about 520 nm through 800 nm, where they can be constrained by the measurements of Anderson & Mauersberger, (1992), and of S.M.Anderson et al., (1993b). At the extreme wavelengths near 407 and 1089 nm, where the cross section becomes very small the uncertainties are driven by sensitivity of the measurements and possible errors in the zero absorption reference value. Near these wavelengths the uncertainties in the data can exceed 25%, decreasing to 10% near 450 nm and to less than 5% near 500 nm. At the longer wavelengths, the uncertainties in the ozone cross sections increase from 2% to 5% between 800 and 850 nm, with a further increase to

about 10% near 950 nm. The recent results of Brion et al. [1998], tend to be systematically higher by 1% than the measurements discussed above.

Burkholder & Talukdar (1994) have provided a very nice measurement of the temperature dependence of the Chappuis band [from 407 to 762 nm], where they use two identical cells to directly measure the ratio of the cross sections at 298 K and a reduced temperature between 220 and 280 K.

The most significant deficiencies in the ozone data for SAGE III are the need to extend the measurements of the temperature dependence to 180 K, to cover the full range of stratospheric temperatures and through the near IR. The latter is needed more to remove ozone as an interfering species from the SAGE measurement of aerosols and water vapor in the near IR as directly to measure ozone. While Burrows et al. (1999) have measured the temperature dependence in out to 794 nm, their room temperature data is systematically higher than either the Shettle & Anderson (1994) compilation or the Brion et al. (1998) measurements throughout the visible. These differences range from 3 to 5 % near the 600 nm Chappuis peak, to in excess of 20% near 750 nm. Also the Burrows et al. (1998) temperature dependence in the visible shows internal inconsistencies.

#### **D.2.1.3 References**

Anderson, G.P., F.X.Kneizys, E.P.Shettle, L.W.Abreu, J.H.Chetwynd, R.E.Huffman, & L.A.Hall (1989), "UV Spectral Simulations Using LOWTRAN 7", in *Atmospheric Propagation in the UV, Visible, IR, & MM-Wave Region and Related Systems Aspects*, AGARD Conference Proceedings No. 454, Proceedings of the AGARD Electromagnetic Wave Propagation Panel Symposium Copenhagen, Denmark, 9-13 October 1989.

Anderson, S.M., P. Hupalo, and K. Mauersberger, "Rotational structure in the near-infrared absorption spectrum of ozone", *J. Chem. Phys.*, 99, 737-739, 1993a.

Anderson, S.M., P. Hupalo, and K. Mauersberger, "Ozone absorption cross section measurements in the Wulf bands", *Geophys. Res. Lett.*, 20, 1579-582, 1993b.

Anderson, S.M., J. Maeder, and K. Mauersberger, "Effect of isotopic substitution on the visible absorption spectrum of ozone", *J. Chem. Phys.*, 94, 6351-6357, 1991.

Anderson, S.M. and K. Mauersberger, "Laser measurements of ozone absorption cross sections in the Chappuis band", *Geophys. Res. Lett.*, 19, 933-936, 1992.

- Anderson, S.M., J. Morton, and K. Mauersberger, "Near-infrared absorption spectra of  $^{16}\text{O}_3$  and  $^{18}\text{O}_3$ : Adiabatic energy of the  $^1\text{A}_2$  state?", *J. Chem. Phys.*, 93, 3826-3832, 1990.
- Barnes, J. & K. Mauersberger (1987), "Temperature Dependence of the Ozone Absorption Cross Section at the 253.7-nm Mercury Line", *J. Geophys. Res.*, 92, 14,861-14,864.
- Bass, A.M. and R.J.Paur (1985), "The ultraviolet Cross-Sections of Ozone. I. Measurements in Atmospheric Ozone", *Proceedings of the Quadrennial Ozone Symposium in Halikidi, Greece*, ed. by C.Zeferos and A.Ghaz, pp 606-616.
- Brion, J. A. Chakir, J. Charbonnier, D. Daumont, C. Parisee, J. Malicet (1998), "Absorption Spectra Measurements for the Ozone Molecule in the 350 to 830 nm Region", *J. Atmos. Chem.*, 30, 291-299.
- Burkholder, J.B. and R.K. Talukdar, "Temperature dependence of the ozone absorption spectrum over the wavelength range 410 to 760 nm", *Geophys. Res. Lett.*, 21, 581-584, 1994.
- Burrows, J.P., A. Richter, A. Dehn, B. Deters, S. Himmelmann, S. Voigt, and J. Orphal, (1999), "Atmospheric remote-sensing reference data from GOME – 2. Temperature-dependent absorption cross sections of  $\text{O}_3$  in the 231-794 nm range", *J. Quant. Spectrosc. Radiat. Transfer*, 61, 509-517.
- Cacciani, M., A.diSarra, and G.Fiocco, (1987), "Laboratory Measurements of the Ozone Absorption Coefficients in the Wavelength Region 339-362 nm at Different Temperatures", Dept. of Physics, University of Roma - La Sapienza, Italy, Internal Note No. 882.
- Cacciani, M., A.diSarra, and G.Fiocco, and A.Amuruso, (1989), "Absolute Determination of the Cross-Sections of Ozone in the Wavelength Region 339-355nm at Temperatures 220-293K", *J. Geophys. Res.*, 94, 8485-8490.
- Daumont, D., J.Brion, J.Charbonnier, & J.Malicet, (1992), "Ozone UV Spectroscopy I: Absorption Cross Sections at Room Temperature", *J. Atmos. Chem.*, 15, 145-155.
- Malicet, J., D. Daumont, J. Charbonnier, C. Parisse, A. Chakir, and J. Brion (1995) "Ozone UV spectroscopy. II Absorption cross-sections and temperature dependence", *J. Atmos. Chem.*, **21**, 263-273.
- Mauersberger, K., J.Barnes, D.Hanson, & J. Morton, (1986), "Measurement of the Ozone Absorption Cross Section at the 253.7 Mercury Line", *Geophys. Res. Lett.*, 13, 671-673.

Mauersberger, K., D.Hanson, J.Barnes, & J. Morton, (1987), "Ozone Vapor Pressure and Absorption Cross Section Measurements: Introduction of an Ozone Standard", *J. Geophys. Res.*, 92, 8480-8485.

Molina, L.T. and M.J.Molina (1986) "Absolute Absorption Cross Sections of Ozone in the 185-350 nm Wavelength Range", *J. Geophys. Res.*, 91, 14,501-14,509.

Shettle, E.P. & S.M.Anderson, (1994), "New Visible and Near IR Ozone Cross Sections for MODTRAN", presented at the 17th Annual Review Conference on Atmospheric Transmission Models, Phillips Laboratory, Bedford, MA 7-8 June 1994.

Yoshino, K. D.E.Freeman, J.R.Esmond, and W.H.Parkinson, (1988) "Absolute Absorption Cross Section Measurements of Ozone in the Wavelength Region 238-335 nm and the Temperature Dependence", *Planet. Space Sci.*, 36, 395-398.

### **D.2.2 Nitrogen Dioxide**

SAGE II has used the NO<sub>2</sub> cross sections measured by Graham & Johnston (1974) and compiled by Goldman et al. (1978) for their retrieval of the NO<sub>2</sub> profiles, (Cunnold et al., 1991). Since then there have been several new measurements of NO<sub>2</sub> absorption cross sections, [Schneider et al., 1987; Davidson et al., 1989; Amoruso et al., 1993; Harwood and Jones, 1994; Mérienne et al., 1995; and Coquart et al., 1995]. Unfortunately intercomparisons of these different data sets with each other and the Graham & Johnston (1974) measurements show differences as large as 1 nm in the position of the minima and maxima of the absorption as a function of wavelength, in addition to differences of up to 10-20 % in the total cross section. One deficiencies of many of these measurements (and most of the earlier ones) is they were made at resolutions of 0.5 to 2 nm which is too coarse to resolve the structure present in the absorption spectrum. Kirmse, et al. (1997) have concatenated several of these earlier measurements to develop a single NO<sub>2</sub> cross section covering 300 to 908 nm. Using the Mérienne et al. (1995) for the 300 to 500 nm region which includes the 420 to 460 nm region used by SAGE III for its NO<sub>2</sub> measurements.

Harder et al. [1997], provide a detailed critical evaluation of the earlier measurements, in addition to high spectral resolution [ $< 0.01$  nm] data of their own, covering 350 to 585 nm, at temperatures between 217 and 298 K. These agree with the University of Reims data to about 4% in absolute cross section. The details of the spectral structure agree although the effects of the aliasing in the Reims data are clearly present.

Recently Yoshino et al. (1997) and Vandaele, et al. (1996 and 1998) have also made high spectral resolution ( $< 0.1$  nm) measurements of the NO<sub>2</sub> cross sections. These all show

agree with the high resolution data of Mérienne et al. (1995) and Harder et al. (1997), to 3 to 5 %. Most of these results include at least one low temperature measurement (except Yoshino et al., 1997). These low temperature measurement also agree to within 5%, with the spectral variations becoming more pronounced. That is the local minima decrease with decreasing temperature and the local maxima increasing with decreasing temperature.

With an instrument such as SAGE II which uses the difference between a single minimum and maximum, the use of a pair where there are large differences between the positions and cross sections, could lead to errors as large as 50 % by using the wrong cross section data. It should be noted that the validation of the SAGE II NO<sub>2</sub> measurements, [Cunnold et al., 1991], indicate that the SAGE NO<sub>2</sub> data is accurate to 15%. SAGE III will retrieve the NO<sub>2</sub> from the structure across several minima and maxima, which should mean it is much less sensitive to the position and cross sections of individual pairs of the minima and maxima. In fact the SAGE III spectral measurements can be used to check for systematic wavelength shifts in the NO<sub>2</sub> absorption data used in the algorithm.

In the spectral region from 400 nm to 460 nm, where there are a number of good quality high resolution measurements available, the uncertainties in the NO<sub>2</sub> absorption cross sections are 3-5 %. This includes the portion of the spectrum used by SAGE III and many other instruments to determine the concentration of NO<sub>2</sub> in the atmosphere. From 300 nm to 400 nm and from 460 nm to 500 nm the uncertainties are 5-7 %. At longer wavelengths, which are still important to remove the contributions of NO<sub>2</sub> from the measurements of other species such as aerosols or NO<sub>3</sub>, the uncertainties are 5-10 %, and are limited to measurements with resolutions (and wavelength accuracies) of 0.5 to 2 nm, which means additional errors will be introduced in convolving them with the spectral response of the SAGE III instrument. The greatest needs for additional measurements are for high resolution data at wavelengths longer than 500 nm and for low temperature measurements at all wavelengths down to 180 K, to cover the full range of stratospheric temperatures.

#### D.2.2.1 References

- Amoruso, A.L., G.Crescentini, G.Fiocco, and M.Volpe, (1993) "New Measurements of the NO<sub>2</sub> Absorption Cross Section in the 440- to 460- nm region and estimates of the NO<sub>2</sub> - N<sub>2</sub>O<sub>4</sub> Equilibrium Constant", *J. Geophys. Res.*, 98, 16,857-16,863.
- Bass, A.M., A.E.Ledford Jr., and A.H.Laufer, "Extinction Coefficients of NO<sub>2</sub> and N<sub>2</sub>O<sub>4</sub>", *J. Res. Natl. Bur. Stand.*, 80A, 143-166.
- Coquart, B. A.Jenouvrier, and M.F.Mérienne (1995) "The NO<sub>2</sub> Absorption Spectrum. II: Absorption Cross-Sections at Low Temperature in the 400-500 nm Region", *J. Atmos. Chem.*, 21, 251-261.



- Cunnold, D.M., J.M.Zwadony, W.P.Chu, J.P.Pommereau, F.Goutail, J.Lenoble, M.P.McCormick, R.E.Viega, D.Murcray, N.Iwagami, K.Shibasaki, P.C.Simon, & W.Peetermans, (1991), "Validation of SAGE II NO<sub>2</sub> Measurements", *J. Geophys. Res.*, 96, 12,913-12,925.
- Davidson, J.A., C.A.Cantell, A.H.McDaniel, R.E.Shetter, S.Madronich, and J.G.Calvert, (1989), "Visible-Ultraviolet Absorption Cross Sections for NO<sub>2</sub> as a Function of Temperature", *J. Geophys. Res.*, 93, 7105-7112.
- Frost, G.J., L.M.Goss, & V.Vaida, (1996) "Measurements of High-Resolution Ultraviolet-Visible absorption Cross Sections at Stratospheric Temperatures: 1. Nitrogen Dioxide", *J. Geophys. Res.*, 101, 3869-3877.
- Graham, R. and H.S.Johnston (1974) "Photochemistry of NO<sub>x</sub> and HNO<sub>x</sub> Compounds", *Can. J. Chem.*, **52**, 1415-1423. [Values tabulated by A.Goldman, U. of Denver]
- Hall, T.C. and F.E. Blacet, (1952) "Separation of the Absorption Spectra of NO<sub>2</sub> and N<sub>2</sub>O<sub>4</sub> in the range 2400-5000 D", *J. Chem. Phys.*, 20, 1745-1749.
- Harder, J.W., J.W.Brault, P.V.Johnston, & G.H.Mount [1997], "Temperature Dependent NO<sub>2</sub> Cross Sections at High Spectral Resolution", *J. Geophys. Res.*, 102, 3861-3879.
- Harwood, M.H. and R.L.Jones (1994), "Temperature Dependent Ultraviolet-Visible Absorption Cross-Sections of NO<sub>2</sub> and N<sub>2</sub>O<sub>4</sub>: Low-Temperature Measurements of the Equilibrium Constant for 2NO<sub>2</sub> ⇌ N<sub>2</sub>O<sub>4</sub>", *J. Geophys. Res.*, 99, 22,955-22,964.
- Mérieulle, M.F., A.Jenouvrier, B.Coquart, (1995) "The NO<sub>2</sub> Absorption Spectrum. I: Absorption Cross-Sections at Ambient Temperature in the 300-500 nm Region", *J. Atmos. Chem.*, 20, 281-297.
- Schneider, W.G., G.K.Moortgat, G.S.Tyndall, and J.P.Burrows, (1987), "Absorption Cross Sections of NO<sub>2</sub> in the UV and Visible Region (200-700 nm) at 298 K", *J. Photochem. Photobiol. A Chem.*, 40, 195-217.
- Vandaele, A.C., C.Hermans, P.C.Simon, M.Carleer, R.Colin, S.Fally, M.F.Mérieulle, A.Jenouvrier, & B.Coquart, (1998) "Measurements of the NO<sub>2</sub> absorption cross-sections from 42,000 cm<sup>-1</sup> to 10,000 cm<sup>-1</sup> (238-1000 nm) at 220 K and 294 K", *J. Quant. Spectrosc. Radiat. Transfer*, 59, 171-184.
- Yoshino, K., J.R.Esmond, W.H.Parkinson, (1997) "High-resolution absorption cross section measurements of NO<sub>2</sub> in the UV and visible region", *Chem. Phys.*, 221, 169-174.

### D.2.3 Oxygen

Accurate knowledge of the oxygen absorption cross sections are critical for the SAGE III Experiment, since the SAGE III oxygen measurements are used to establish the atmospheric density, temperature, and pressure profiles. In addition to the direct scientific need for these profiles, they are also needed to remove the molecular Rayleigh scattering contribution from the measurements of other species at all wavelengths, and for the retrieval of the mixing ratio of the other gaseous species on pressure surfaces. This removes the need for external source of this data, such as the NMC analyses which were used for the SAGE I and II instruments. To retrieve the oxygen density, from which the atmospheric density, temperature, and pressure profiles will be derived, SAGE III will use differential absorption measurements across the oxygen A band from 755 to 775 nm.

The Ritter & Wilkerson (1986) measurements of the oxygen A band with a stated accuracy of about 2%, appear to be the best of the available data. They have been adapted by Chance (1995) for use with the Global Ozone Monitoring Experiment (GOME). However, their band strength is higher than all of the previous measurements that they include in their Table IV, exceeding the next highest by nearly 5%, the mean by 11%, and exceed by 15% the data of Miller et al. (1969), (with a stated accuracy of 4%), which are the basis of the 1992 HITRAN database, (Rothman et al., 1992). Ritter & Wilkerson's (1986) line widths are near the middle of the range of the previous measurements, which have a 30% range of values. However, while the 1996 HITRAN database adapted the Ritter & Wilkerson (1986) line strengths, it continues to utilize the line widths of Givers et al. (1974), which are at the low end of the available measurements.

Recently Brown and Plymate (1999) have measured the oxygen A band. The line positions, line intensities and pressure-broadening coefficients of 44 transitions in the oxygen A-band near 760 nm (from 13040 to 13168  $\text{cm}^{-1}$ ) have been calibrated using laboratory data recorded at 0.02  $\text{cm}^{-1}$  resolution with the Fourier transform spectrometer at Kitt Peak in Arizona. The pressure-broadening coefficients for self- and nitrogen-broadened widths and pressure-induced shifts in line positions have been measured through  $J'' = 24$ ; these have been combined and modeled with a polynomial expressed as a function of the upper state quantum number in order to compute the corresponding air-broadened line shape coefficients associated with Voigt profiles. The temperature dependence of the line widths has been determined from absorption spectra obtained with gas samples temperatures between 205 K and 297 K

The measured intensities demonstrate that the values selected for the 1996 HITRAN database are valid to within 1%. However, the line positions are in error by 0.002 to 0.015  $\text{cm}^{-1}$  and the widths by 7 to 20%. Although the individual new measurements of temperature dependence of widths have uncertainties of 15%, the average of new measured values is within 2% of the mean value previously selected by HITRAN.

### D.2.3.1 References

- Brown, L.R. and C. Plymate, (1999) "Experimental line parameters of the oxygen A-band at 760 nm.", *submitted to J. Mol. Spectrosc.*
- Brown, L.R. and R.A.Toth (1995) "Laboratory Spectroscopy of SAGE Molecules", Unpublished Manuscript.
- Chance, K., (1995) "O<sub>2</sub> A Band Studies for Cloud Detection and Algorithm Improvement" (1995), Contact Report for ESA.
- Giver, L.P., R.W.Boese, & J.H.Miller (1974) "Intensity Measurements, Self-Broadening Coefficients, and Rotational Intensity Distribution for Lines of the Oxygen B Band at 6880 C", *J. Quant. Spectrosc. Radiat. Transfer*, 14, 793-802.
- Miller, J.H., R.W.Boese, & L.P.Giver (1969) "Intensity Measurements and Rotational Intensity Distribution for the Oxygen A Band", *J. Quant. Spectrosc. Radiat. Transfer*, 9, 1507-1517.
- Newnham, D.A., and J. Ballard (1998) "Visible absorption cross sections and integrated absorption intensities of molecular oxygen (O<sub>2</sub> and O<sub>4</sub>)", *J. Geophys. Res.*, 103, 28,801-28,816.
- Ritter, K.J. and T.D.Wilkerson (1987), "High Resolution Spectroscopy of the Oxygen A Band", *J. Molec. Spectrosc.*, 121, 1-19
- Rothman, L.S., R.R.Gamache, R.H.Tipping, C.P.Rinsland, M.A.H.Smith, D.C.Benner, V.M.Devi, J.-M.Flaud, C.Camy-Peyret, A.Perrin, A.Goldman, S.T.Massie, L.R.Brown, & R.A.Toth, (1992) "The HITRAN Molecular Database Editions of 1991 and 1992", *J. Quant. Spectrosc. Radiat. Transfer*, 48, 469-507.
- Rothman, L.S. C.P. Rinsland, A. Goldman, S.T. Massie, D.P. Edwards, J.-M. Flaud, A. Perrin, C. Camy-Peyret, V. Dana, J.-Y. Mandin, J. Schroeder, A. McCann, R.R. Gamache, R.B. Watson, K. Yoshino, K.V. Chance, K.W. Jucks, L.R. Brown, V. Nemtchinov, and P. Varanasi (1998), "The HITRAN molecular spectroscopic database and HAWKS (HITRAN Atmospheric WorkStation): 1996 edition", *J. Quant. Spectrosc. Radiat. Transfer*, 60, 665-710.

### D.2.4 Water Vapor

To measure atmospheric water vapor SAGE III will use differential absorption in the near IR water band from 920 to 960 nm. The HITRAN database, Rothman (1992), based on

the measurements of Chevillard et al. (1989), provides the best available spectroscopic data, in this region. This is an improvement over the 1982 edition of the HITRAN database used by Chu et al. (1993) for the water vapor retrievals from SAGE II. However as noted by Brown and Toth (1995), this band is a complex of 10 interacting vibrational states and a complete theoretical modeling has not been accomplished to date, limiting the ability to give a complete accurate listing of the line positions, intensities, and spectral assignments. Recently Giver et al. (1999) have reported that there were systematic errors in implementing the line intensities of water vapor into the HITRAN database, which affects all the visible and near IR water bands with wavelengths less than 1200 nm. For the band centered around 940 nm, which will be by SAGE III to retrieve water vapor, this correction amounts to a 14.4 % increase in all the lines derived from the data of Chevillard et al. (1989). Which applies to most of the lines in this band. There are number of weak lines in this region due to  $\text{H}_2^{17}\text{O}$  and  $\text{H}_2^{18}\text{O}$ , and a few unassigned lines. It is presently not clear whether this correction applies to any of these lines, however altogether they contribute only about 1% of the total band strength.

The reported accuracies of the Chevillard et al. (1989) data are 7 to 50 %, depending on the spectral line. Given the 50 % uncertainties apply to the weakest lines, when integrated over the 2 nm resolution of the SAGE III detector, the water vapor absorption is known to about 10 to 15 %. To achieve greater accuracy for water vapor retrievals will require new measurements of the water vapor spectroscopy in the near IR.

Recently Brown et al. (1999, unpublished manuscript), have obtained new measurements of the water vapor lines for the 940 nm band. The line positions and line intensities of some 2600 transitions have been retrieved from 17 absorption spectra recorded at 0.01 and 0.02  $\text{cm}^{-1}$  resolution using the Fourier transform spectrometer at Kitt Peak in Arizona. These have been combined with published analyses for isotopic water ( $\text{H}_2\text{-}^{16}\text{O}\text{-}^{18}\text{O}$  and  $\text{H}_2\text{-}^{16}\text{O}\text{-}^{17}\text{O}$ ) to produce a new line list of some 4130 transitions from 9676.8789 to 11386.2119  $\text{cm}^{-1}$ . Available air-broadened and self-broadened line widths from other vibrational bands at 6  $\mu\text{m}$  and 2.1  $\mu\text{m}$  have been inserted for A- and B- type transitions of bands in the 0.96  $\mu\text{m}$  region. There are no new data for pressure-shifts and temperature dependences, however.

This study will correct the conversion mistakes recently uncovered in the visible line parameters of water by COMPLETELY REPLACING the current 0.96  $\mu\text{m}$  list in HITRAN and GEISA with better quality measurements (0.001  $\text{cm}^{-1}$  for positions and 3% for the intensities). The individual intensities range from  $6.5 \times 10^{-22}$  to  $1 \times 10^{-27} \text{ cm}^{-1}/(\text{molecule} \times \text{cm}^{-2})$  at 296 K.

#### D.2.4.1 References

- Brown, L.R. and R.A.Toth (1995) "Laboratory Spectroscopy of SAGE Molecules", Unpublished Manuscript.
- Chevillard, J.-P., J.-Y.Mandin, J.-M.Flaud, & C. Camy-Peyret (1989) "  $\text{H}_2^{16}\text{O}$ : Line positions and intensities between 9500 and 11500  $\text{cm}^{-1}$ . The interacting vibrational states (041), (220), (121), (022), 9300), (201), (102), and (003)", *Can. J. Phys.*, 67, 1065-1084
- Chu, W.P., E.W.Chiou, J.C.Larsen, L.W.Thomason, D.Rind, J.J.Buglia, S.Oltsman, M.P.McCormick, & L.M.McMaster (1993) "Algorithms and sensitivity analyses for Stratospheric Aerosol and Gas Experiment II water vapor retrieval", *J. Geophys. Res.*, 98, 4857-4866.
- Giver, L.P., C. Chackerian, and P. Varanasi, "Visible and Near-Infrared  $\text{H}_2^{16}\text{O}$  Line Intensity Corrections for HITRAN-96", *to be published in J. Quantat. Spectrosc. Radiative Transf.*, 1999.
- Rothman, L.S., R.R.Gamache, R.H.Tipping, C.P.Rinsland, M.A.H.Smith, D.C.Benner, V.M.Devi, J.-M.Flaud, C.Camy-Peyret, A.Perrin, A.Goldman, S.T.Massie, L.R.Brown, & R.A.Toth, (1992) "The HITRAN Molecular Database Editions of 1991 and 1992", *J. Quant. Spectrosc. Radiat. Transfer*, 48, 469-507.
- Rothman, L.S., R.R.Gamache, A.Barbe, A.Goldman, J.R.Gillis, L.R.Brown, R.A.Toth, J.-M.Flaud, & C.Camy-Peyret (1983) "AFGL atmospheric absorption line parameters compilation: 1982 edition", *Appl. Opt.*, 22, 2247-2256.
- Rothman, L.S. C.P. Rinsland, A. Goldman, S.T. Massie, D.P. Edwards, J.-M. Flaud, A. Perrin, C. Camy-Peyret, V. Dana, J.-Y. Mandin, J. Schroeder, A. McCann, R.R. Gamache, R.B. Watson, K. Yoshino, K.V. Chance, K.W. Jucks, L.R. Brown, V. Nemtchinov, and P. Varanasi (1998), "The HITRAN molecular spectroscopic database and HAWKS (HITRAN Atmospheric WorkStation): 1996 edition", *J. Quant. Spectrosc. Radiat. Transfer*, 60, 665-710.

#### D.2.5 The Nitrate Free Radical $\text{NO}_3$

SAGE III utilizing differential absorption spectroscopy in the 640 to 680 nm region will measure the nitrate free radical  $\text{NO}_3$ . It is at least a weak absorber throughout the visible, although strong absorption features and 623 and 662 nm dominate its visible spectrum. A

general review of the Nitrate Free Radical  $\text{NO}_3$ , including its spectroscopy, is given by Wayne et al. (1991)n.

DeMore et al. (1997) recommend using an average of the studies by Marinelli et al. (1982), Ravishankara & Wine (1983), Burrows et al. (1985), Ravishankara & Mauldin (1986), Sander (1986), Canosa-Mas et al. (1987), and Cantrell et al. (1987) for the cross section at the 662 nm peak at room temperature. There is disagreement in the temperature dependence with Cantrell et al. (1987) finding the absorption to be independent of temperature between 215 and 348 K, and Ravishankara & Mauldin (1986) and Sander (1986) reporting the cross section increasing with decreasing temperature. For the cross section increase, Ravishankara & Mauldin report 40 % between 298 and 220 K and Sanders 20 % between 298 and 230 K. The recent measurements of Yokelson et al. (1994) tend to support the temperature dependence of Sanders. Yokelson et al. also note that their measurements can be considered to supersede the earlier results of Ravishankara & Mauldin (1987).

The uncertainties in the absorption cross sections are 10-15 % at room temperature and 20-25 % at stratospheric temperatures. Given this results in a corresponding uncertainty of the retrieved  $\text{NO}_3$  amounts, improved measurements are needed.

#### D.2.5.1 References

Burrows, J.P., G.S.Tyndall, & G.K.Moortgat (1985) "Absorption spectrum of  $\text{NO}_3$  and kinetics of the reactions of  $\text{NO}_3$  with  $\text{NO}_2$ , Cl, and several stable atmospheric species at 298 K", *J. Chem. Phys.*, 89, 4848-4856.

Canosa-Mas, C.E., M.Fowles, P.J.Houghton, & R.P.Wayne (1987) "Absolute absorption cross section measurements on  $\text{NO}_3$ ", *J. Chem. Soc. Faraday Trans. II*, 83, 1465-1474.

Cantrell, C.A., J.A.Davidson, R.E.Shetter, B.A.Anderson, & J.G.Calvert (1987) "The temperature Invariance of the  $\text{NO}_3$  absorption cross section in the 662 nm region", *J. Phys. Chem.*, 91, 5858-5863.

DeMore, W.B., S.P. Sander, D.M.Golden, R.F.Hampson, M.J.Kurylo, C.J.Howard, A.R.Ravishankara, C.E.Kolb, M.J.Molina (1994), *Chemical Kinetics and Photochemical Data for Use in Stratospheric Modeling Evaluation Number 11*, JPL Publication 94-26

DeMore, W.B., S.P. Sander, D.M.Golden, R.F.Hampson, M.J.Kurylo, C.J.Howard, A.R.Ravishankara, C.E.Kolb, M.J.Molina (1997), *Chemical Kinetics and*

- Marinelli, W.J., D.M.Swanson, & H.S.Johnston (1982) "Absorption cross sections and line shape for the NO<sub>3</sub> (0-0) band", *J. Chem. Phys.*, 76, 2864-2870.
- Ravishankara, A.R. & R.L.Mauldin III (1986) "Temperature dependence of NO<sub>3</sub> cross section in the 662-nm region", *J. Geophys. Res.*, 91, 8709-8712.
- Ravishankara, A.R. & P.H.Wine (1983) "Absorption Cross Sections for NO<sub>3</sub> between 565 and 673 nm", *Chem. Phys. Lettr.*, 101, 73-78.
- Sanders, S.P. (1986) "Temperature dependence of the NO<sub>3</sub> absorption spectrum", *J. Chem. Phys.*, 90, 4135-4142.
- Wayne, R.P., I.Barnes, P.Biggs, J.P.Burrows, C.E.Canosa-Mas, J.Hjorth, G. Le Bras, G.K.Moortgat, D.Perner, G.Poulet, G.Restlli, & H.Sidebottom (1991) "The Nitrate Radical: Physics, Chemistry, and the Atmosphere", *Atmos. Environ.*, 25A, 1-203.
- Yokelson, R.J., J.B. Burkholder, R.W. Fox, R.K. Talukdar, and A.R. Ravishankara, "Temperature Dependence of the NO<sub>3</sub> Absorption Spectrum", *J. Phys. Chem.*, 98, 13,144-150, 1994.

#### **D.2.6 Symmetric Chlorine Dioxide OClO**

Symmetric chlorine dioxide, OClO, has series of absorption peaks between 280 and 480 nm, which reach a maximum near 351 nm. The region from 380 to 420 nm will be used for the SAGE III retrievals of OClO. While there have been a number of spectroscopic studies of OClO, relatively few experiments have provided absolute cross sections at room temperature, with apparently only Wahner et al. (1987) examining the temperature dependence. Frost et al. (1996) have recently reported a spectroscopic study of OClO at stratospheric temperatures (200 +/- 20 K) however, using two different techniques to convert this data to absolute cross sections, report differences of 50%. DeMore et al. (1994) recommend the Wahner et al. (1987) absorption cross sections. These data have a reported accuracy of 3-5 %.

#### D.2.6.1 References

- DeMore, W.B., S.P. Sander, D.M. Golden, R.F. Hampson, M.J. Kurylo, C.J. Howard, A.R. Ravishankara, C.E. Kolb, M.J. Molina (1994), *Chemical Kinetics and Photochemical Data for Use in Stratospheric Modeling Evaluation Number 11*, JPL Publication 94-26
- Frost, G.J., L.M. Goss, & V. Vaida, (1996) "Measurements of High-Resolution Ultraviolet-Visible absorption Cross Sections at Stratospheric Temperatures: 2. Chlorine dioxide", *J. Geophys. Res.*, 101, 3879-3884.
- Wahner, A., G.S. Tyndall, & A.R. Ravishankara (1987) "Absorption cross sections for OClO as a function of temperature in the wavelength range 240-480 nm", *J. Phys. Chem.*, 91, 2734-2738.



## **Appendix E. Lunar Altitude Registration**

The tangent height registration for the lunar radiometric measurements can be accomplished using a technique similar to the solar method described in the SAGE III Algorithm Theoretical Basis Document, Transmission Level 1B Products, Section 3.2.3. To accomplish the tangent height registration, the primary requirement is to accurately determine the position on the lunar limb, in angular units, of the measurement position. Meeting this requirement is complicated by the scanning motion of the instrument field of view over the target (moon), resulting in the radiometric measurements being taken at irregular points on the target limb, and the absence of accurate absolute pointing information from the instrument. Additionally, the instrument is designed to focus the scan plane through the radiometric center of the moon, which, unlike the case of the sun as the target, does not coincide with the geometric center of the moon. Information provided by the instrument used in the calculations to meet the limb position registration requirement includes the time of the radiometric measurement and the accurate relative pointing information derived from the movement of the instrument scan mirror. At each time increment, a detailed ephemeris calculation can be accomplished that solves the geometry data parameters for the spacecraft to Earth and moon. These ephemeris calculations provide the geometry position information from the spacecraft to the moon center, top, and bottom limbs.

To perform the tangent height registration, additional information will be required from a radiance model of the moon. Information required from the model includes the radiance center, terminator location, and rotation to the scan plane of the instrument. A radiance model is currently being developed as part of the NASA Earth Observing Spacecraft Mission by the U.S. Geological Survey and Northern Arizona University as Project ROLO. The radiance map of the moon, required as an input to the SAGE III model, could be the Project ROLO data when it becomes available, or some alternative to-be-determined source.

The tangent height computations are accomplished using the following steps:

1. A radiometric model predicts the radiometric center of the moon and establishes whether the upper or lower limb of the moon is inside the lunar terminator line.
2. The scan azimuth angle in angular units relative to the target is determined by the difference between the ephemeris calculated velocity to target angle and the measured relative azimuth change of the instrument.
3. An edge signature is established and used to accurately locate the first observation that falls on the top or bottom edge of the lunar disk. The edge signature is established using the second derivative inflection point as the edge crossing time.

4. A geometric height correction is calculated for the first observation based on the offset of the radiometric center of the moon from the geometric center of the moon, and the scan azimuth angle. The geometric height correction, in angular units, is applied to the first observation to correct for the height difference between the (known) height of the top (or bottom) of the lunar disk and the offset height of the first observation.
5. Relative scan mirror elevation movement is used to calculate the angular positions of the subsequent observation points on the lunar limb.
6. The refracted tangent altitude of each observation point is then computed from the angular positions using the same processing routine as the solar processing procedure.